Collapse of Eurasian ice sheets 14,600 years ago was a major source of global Meltwater Pulse 1a

Jo Brendryen[1,2,3,*], Haflidi Haflidason[1,2], Yusuke Yokoyama[4], Kristian Agasøster Haaga[1,2,3], and Bjarte Hannisdal[1,2,3]

[1]*Department of Earth Science, University of Bergen, Norway*
[2]*Bjerknes Centre for Climate Research, University of Bergen*
[3]*K.G. Jebsen Centre for Deep Sea Research, University of Bergen*
[4]*Atmosphere and Ocean Research Institute, University of Tokyo, Japan*
[*]Corresponding author: *jo.brendryen@uib.no*

Rapid sea-level rise caused by the collapse of large ice sheets is a global threat to human societies[1]. In the last deglacial period, the rate of global sea-level rise peaked at more than 4 cm/yr during Meltwater Pulse 1a, which coincided with the abrupt Bølling warming event ~14,650 yr ago[2–5]. However, the sources of the meltwater have proven elusive[6,7], and the contribution from Eurasian ice sheets has until now been considered negligible[8–10]. Here we show that marine-based sectors of the Eurasian ice sheet complex collapsed at the Bølling transition and lost an ice volume of between 4.5 and 7.9 m sea level equivalents (95% quantiles) over 500 yr. During peak melting 14,650 - 14,310 yr ago, Eurasian ice sheets lost between 3.3 and 6.7 m sea level equivalents (95% quantiles), thus contributing significantly to Meltwater Pulse 1a. A mean meltwater flux of 0.2 Sv over 300 yr was injected into the Norwegian Sea and the Arctic Ocean during a time when proxy evidence suggests vigorous Atlantic meridional overturning circulation[11,12]. Our reconstruction of the EIS deglaciation shows that a marine-based ice sheet comparable in size to the West Antarctic ice sheet can collapse in as little as 300-500 years.

Understanding the response of marine-based ice sheets to global warming is critical to future sea-level projections[1]. Today large marine-based ice sheets are situated in the Antarctic, with the West Antarctic ice sheet long considered to be particularly vulnerable[13–16]. The time scale and magnitude of its potential disintegration are highly uncertain, however, and its projected contribution to sea-level rise over the next centuries varies by orders of magnitude[17,18]. To add further empirical constraints, researchers turn to past deglaciation events to study the tempo and mode of ice sheet collapse in a warming world. The West Antarctic ice sheet itself survived the end of the last ice age, but an important analogue can be found in the collapse of the Late Pleistocene Eurasian ice sheet complex (EIS) (Fig. 1).

During the last glacial maximum, 20-21 kyr ago, the EIS attained a maximum ice volume of ~24 m global sea level equivalents (SLE)[19], including large marine-based sectors extending all the way to the continental shelf edge. These sectors formed an extensive interface to the Arctic Ocean and the Nordic Seas, which are one of the main loci of deep-water formation essential to the Atlantic Meridional Overturning Circulation (AMOC). This region is thus of particular importance for understanding the impact of meltwater forcing on ocean circulation and global climate[20].

At the end of the last ice age, abrupt Northern Hemisphere warming at the Bølling transition ~14,650 yr BP coincided with accelerated melting of ice sheets in an event known as global Meltwater Pulse 1a (MWP-1a)[2–5]. During this event, mean global sea-level rose by 12-14 m in ~340 yr, at a rate of at least 4 cm/yr[5]. The sources, magnitude and timing of the MWP-1a have been a subject of controversy over the past decades, and a significant role for the EIS has until now been largely dismissed[6,8,10]. Previous reconstructions of the EIS deglaciation and meltwater contributions[8,19,21] have concluded that the bulk of the marine sectors were deglaciated well before the Bølling transition and the MWP-1a. These reconstructions have, however, assumed a constant marine radiocarbon reservoir age (R) similar to the modern value throughout the deglaciation, typically around 400 yr. Although the uncertainty of this assumption is commonly acknowledged, a lack of constraints on the temporal evolution of R in the Norwegian Sea has prevented a more accurate reconstruction of the deglaciation.

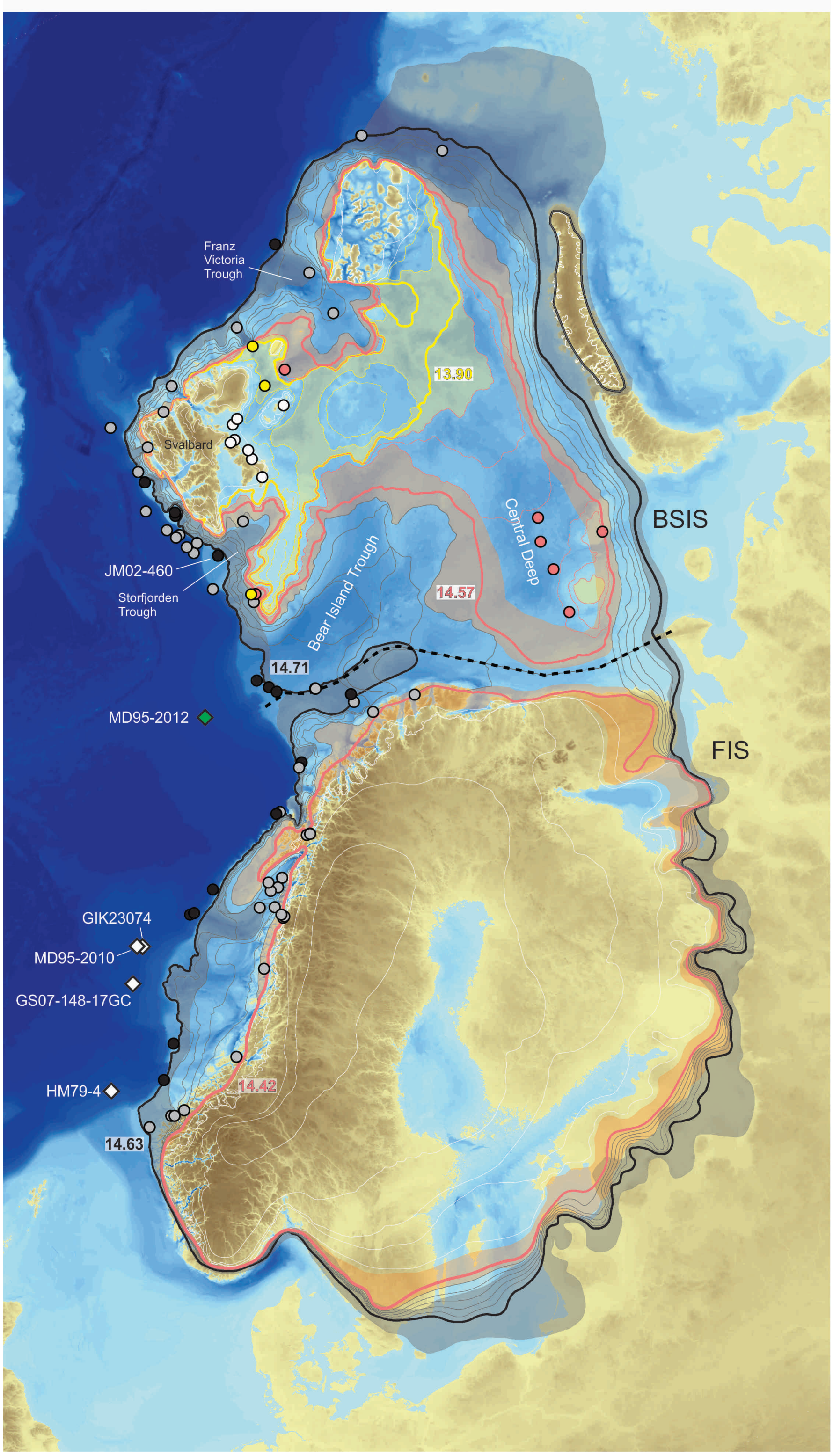

Figure 1: Reconstructed Late Pleistocene EIS complex comprised of the Fennoscandian Ice Sheet (FIS) and the Barents-Svalbard Ice Sheet (BSIS). Contour lines represent ice margins at different stages of the deglaciation. Thick lines represent ice margin positions at boundaries between the deglacial phases used in the Bayesian chronology (Supplementary Data Fig. 8 and 9 and Supplementary Data File). Black lines are the inferred ice margin following the late Heinrich Stadial 1 ice advance. Pink lines are the ice margins that followed the separation of the BSIS and FIS. Yellow lines mark ice margins when the BSIS are constrained on the archipelagos and shallow banks in the northern Barents sea. The median age of each margin is indicated. The accompanying transparent fields mark the geographic uncertainties associated with the respective ice margins. Thin lines mark the suggested ice sheet retreat pattern within each phase as synthesized from the literature listed in Methods. The black stippled line marks the separation between the FIS and the BSIS used in the area-volume calculation when they were confluent. Black filled circles mark sites used to constrain the Heinrich Stadial 1 extent of the ice sheet. The positions of the stratigraphic records and dates used to constrain the deglacial phases are marked with gray, pink, yellow and white filled circles. White diamonds mark the position of cores used to reconstruct the Norwegian Sea ^{14}C reservoir age. White lines indicate ice margins adopted from the Dated-1 reconstruction.

Norwegian Sea ^{14}C reconstruction and deglacial chronology

We here present a new chronology for the deglaciation of the marine-based sectors of the EIS complex, using new constraints on the Norwegian Sea ^{14}C and R to calibrate marine ^{14}C dates linked to the retreat of the EIS. We take advantage of the close connection between North Atlantic climate and the Asian Monsoon[22–27] to align Norwegian Sea paleoceanographic records with a U/Th-dated speleothem record from Hulu Cave, China[28,29] (Fig. 2; Methods; Supplementary Fig. 1). This alignment is corroborated by a tephrochronological marker bed found both in Norwegian Sea sediments and Greenland ice cores (Supplementary Fig. 1, Methods). To assess the robustness of our reconstruction, we used an alternative age model based on the Vedde Ash and 24 ^{14}C dates compiled from the Younger Dryas and the Bølling-Allerød intervals, for which the Norwegian Sea R has been independently constrained by paired marine and terrestrial ^{14}C dates[30]. This alternative age model does not depend on any tuning of paleoclimatic proxy records and does not assume any climatic teleconnections, yet it results in a ^{14}C reconstruction that falls within the 68.2 % credible intervals of our original reconstruction (Supplementary Fig. 3). Hence, our reconstructed Norwegian Sea ^{14}C record is robust, and our conclusions do not rest on the interpretation of individual proxy records. The ^{14}C age difference between 99 ^{14}C dates compiled from the Norwegian Sea cores and the corresponding atmospheric ^{14}C age represented by the IntCal13 calibration curve[31] (Fig. 2F) yields a new and detailed account of the temporal evolution of the Norwegian Sea ^{14}C reservoir age from 19,000 to 12,500 yr BP (Fig. 2G).

Prior to the Bølling warming, the Norwegian Sea had a mean R of 1,620 ^{14}C yr (Fig. 2G). Then, at the Bølling transition, R abruptly declined by ~1,500 ^{14}C yr in less than 400 calendar yr and the mean R for the remainder of the warm period was 420 ^{14}C yr (Fig. 2). We resample (Methods) the compiled timeseries of ^{14}C ages by a Monte Carlo technique where chronological, stratigraphical and ^{14}C uncertainties are taken into account (Fig. 2F) and use this to calibrate published conventional radiocarbon ages from sedimentary archives that are linked to the dynamics and deglaciation of marine-based sectors of the EIS. The deglaciation of the EIS complex is reconstructed using a probabilistic approach, taking into account uncertainty in both area and age (Methods). The resulting estimates are reported here as medians and 95% quantiles from the probability distributions. The deglaciation for the BSIS and FIS is constrained independently, yielding a sequence of reconstructed ice margins with uncertainty bounds (Fig. 1).

Our revised EIS chronology (Supplementary Figs. 8 and 9; Supplementary Data File) suggests that the Barents-Svalbard ice sheet (BSIS) remained in an advanced position until 14.71 (14.81-14.63) kyr cal BP, after which it rapidly retreated from the outer shelf and deeper troughs at the Bølling transition. At 14.57 (14.67-14.46) kyr cal BP, the BSIS had separated from the Fennoscandian ice sheet, forming an ice lobe over the Central Deep in the Barents Sea, and by 13.90 (14.20-13.57) kyr cal BP it had become confined to islands and shallow banks in the northern Barents Sea (Fig. 1). The reconstructed retreat of the BSIS is congruent with a prominent early Bølling meltwater δ^{18}O anomaly observed in proxy records from core MD95-2012 retrieved from the Barents Sea margin[37,38]. Deglaciation of the Fennoscandian ice sheet commenced at 14.63 (14.78-14.49) kyr cal BP, and by 14.42 (14.57-14.20) kyr cal BP it had retreated from the continental shelf into the coastal areas (Fig. 1).

EIS collapse and MWP-1a contribution

Based on the area-volume relationship for extant ice sheets[39], our reconstruction implies that before the Bølling transition, the EIS contained an ice volume of 15.0 (13.9-16.1) m SLE (Figure 2H). We also applied an alternative area-volume regression using the output of a transient model of the EIS complex itself[40] (Supplementary Fig. 10). Although the alternative regression yields an EIS volume that is 2.7 m SLE less than the Paterson approximation at the start of the deglaciation, the estimated ice loss between 14.7 and 14.4 kyr BP differs by only ~0.2 m SLE, which is negligible with respect to our conclusions. Hence, our mass loss estimates are robust to the assumptions of the area-volume conversion (Supplementary Fig. 10).

Our new reconstruction implies that the marine-based EIS collapsed at the Bølling transition. Over a 500 yr period, starting at 14.71 cal kyr BP, the EIS lost a volume of 6.2 (4.5-7.9) m SLE. Within the MWP-1a time span as defined by the Tahiti chronology (14.65-14.31 kyr BP)[5], the EIS lost a volume of 4.9 (3.3-6.7) m SLE, implying that the collapse of the EIS was a major source of the MWP-1a. Given the presence of ichnofabric in parts of the Norwegian Sea core sediments, we show that bioturbation would result in the smearing out of a more abrupt change in the reservoir age occurring close to the Bølling transition, effectively shifting the start of the R decline back in time by more than 200 calendar years (Methods; Supplementary Fig. 7). Therefore, our mass loss estimates are likely to be conservative, in the

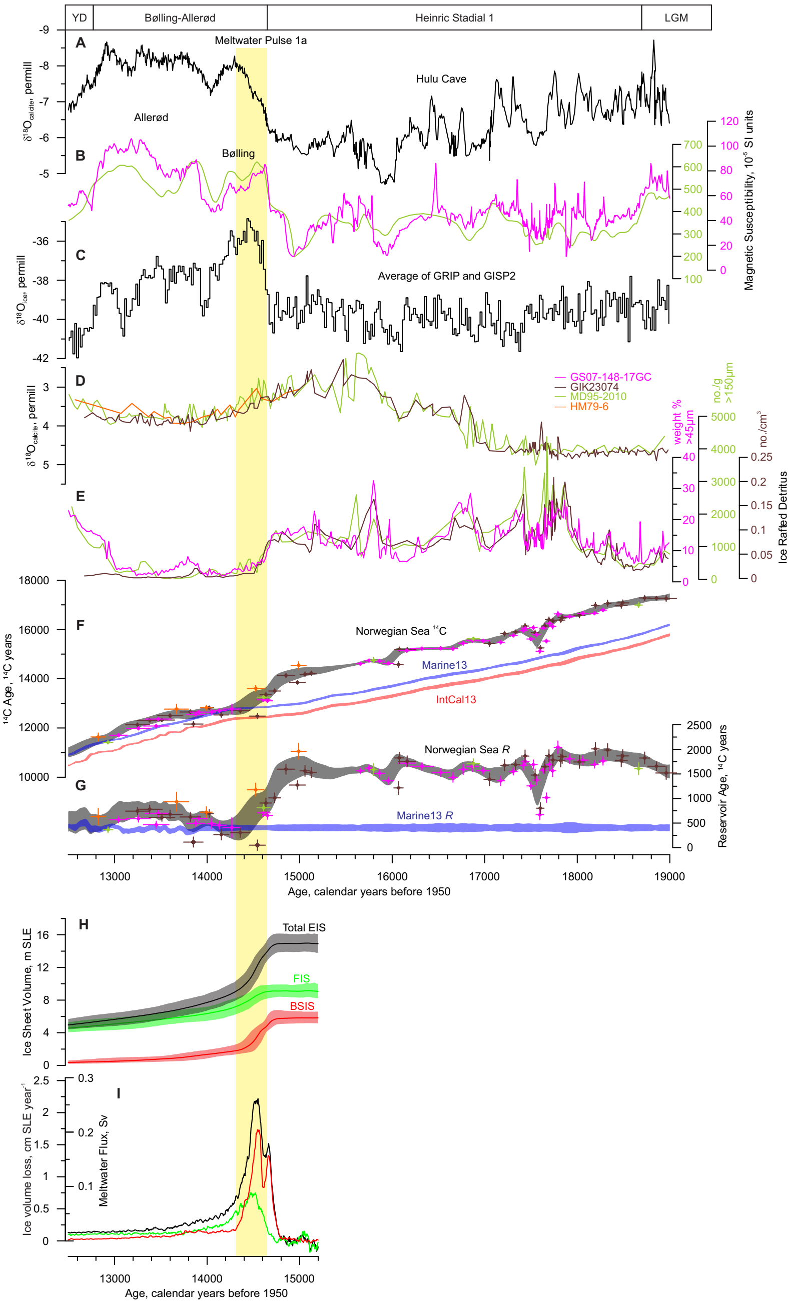

Figure 2: Records of climate, ice volume and meltwater flux from the Eurasian Ice Sheet complex. **A**, δ^{18}O record from Hulu cave speleothem H82,[22,28,29]. **B**, Magnetic susceptibility from Norwegian Sea cores GS07-148-17GC (magenta) and MD95-2010[32] (green) (Fig. 1), aligned with the speleothem δ^{18}O record in **(A)** (Methods). **C**, Average δ^{18}O record from Greenland summit ice cores (GISP2 and GRIP) on the GICC05 chronology[33]. **D**, Planktonic foraminifera δ^{18}O (*Neoglobigerina pachyderma* sinistral) from three Norwegian Sea sediment cores[32,34,35]. **E**, Proxy records of ice rafted detritus from Norwegian Sea cores[32,34]. **F**, Compiled AMS ^{14}C ages from Norwegian Sea sediment cores (GS07-148-17GC, this study; GIK23074[34,36]; MD95-2010[32]; HM79-6[35]). Horizontal error bars represent the 68.2% quantiles (equivalent to 1σ) of the GS07-148-17GC deposition model. Gray shading represents $\pm1\sigma$ of the Monte Carlo sampling of the probability density functions of both the stratigraphic and chronological core alignments and the ^{14}C uncertainty. **G**, Norwegian Sea ^{14}C reservoir age, R is calculated as the difference between the conventional ^{14}C ages (at the median age) and the IntCal13 atmospheric ^{14}C curve[31]. Vertical error bars are the root sum of squares of the ^{14}C uncertainties. The average global reservoir age represented by the Marine13 calibration curve[31] is plotted for reference. **H**, Reconstructed ice volume for the Eurasian Ice Sheet (EIS) complex expressed as m sea level equivalents (SLE; 25 yr running mean of median and 95% quantiles). FIS: Fennoscandian Ice Sheet; BSIS: Barents-Svalbard Ice Sheet. I: median rate of ice volume loss in cm SLE per yr and as meltwater flux (Sv) (colors as in **(H)**).

sense that they may overestimate the time span of the EIS collapse and thus underestimate its contribution to the MWP-1a.

Implications for deglaciation and ice sheet collapse

An EIS contribution of 4.9 (3.3-6.7) m SLE to the MWP-1a is substantially larger than previous estimates in Dated-1[19] (1.1 m SLE when interpolated to 340 yr from the most-credible Dated-1 ice margins at 15 and 14 kyr BP), and is comparable to the estimated contribution from the much larger North American ice sheet (5-6 m SLE in ref.[41], 6.4-9 m SLE (interpolated to 340 yr) in ref.[42], and 4-7 m SLE in ref.[10]). Although a prominent MWP-1a contribution from the EIS is consistent with observed far-field sea-level fingerprints[9], the inferred total amplitude of the MWP-1a and the distribution of other meltwater sources need to be reconsidered in light of our findings[5,6].

Modeled far-field sea-level fingerprints suggest that a MWP-1a sourced from the EIS would amplify the local relative sea-level rise (RSL) by about 10 % at Tahiti and by 4 % at the Sunda shelf relative to the eustatic rise[9]. This proportional increase would translate our conservative estimates of EIS mass loss during the MWP-1a into 3.6-7.4 m RSL rise at Tahiti and 3.3-7.0 m RSL rise at the Sunda shelf. If we consider the observed low-end RSL rise of 12 m at Tahiti[5], then our results suggest that the EIS collapse may have contributed 30-60 % of the MWP-1a local sea level rise at this locality. For the high-end MWP-1a RSL rise estimate of 17.3 m at the Sunda shelf[6], our mass loss estimates correspond to 20-40% of the local sea level rise. A more accurate estimate of the eustatic sea-level contribution from the EIS collapse will require additional constraints on the effect of glacio-isostasy and ice volume below flotation. Nevertheless, our findings provide strong empirical evidence that the EIS was a major source of the MWP-1a. Combined with recent estimates for the North American Ice Sheet MWP-1a contribution[10,42] our EIS mass loss estimates are sufficient for explaining the far-field RSL observations without a major Antarctic contribution, consistent with the lack of field evidence for a large retreat of the Antarctic Ice Sheet[43].

In the proximity of a disintegrating ice sheet, the loss of gravitational attraction, as well as crustal rebound, will dominate relative to eustatic sea-level rise, causing RSL to fall[44]. Our results imply that the magnitude of MWP-1a RSL fall would increase towards the Barents Sea, where the EIS mass loss was centred, and decrease towards the south, where the MWP-1a mass loss from the Fennoscandian ice sheet was smaller (Figs. 1 and 2). Available Norwegian RSL observations that extend into the Bølling are consistent with this expected pattern: In western Finnmark, bordering the Barents Sea, estimated Bølling-Allerød RSL fall is ~40m[45]. In Southern Norway, RSL reconstructions suggest a fall of ~15m in Sunnmøre[46], and ~10m or less in south-western Norway[47,48]. A large MWP-1a contribution from the nearby EIS would also help resolve the apparent discrepancy between observed records of a Bølling RSL fall in Scotland and predictions of RSL rise based on glacioisostatic models of the MWP-1a sourced predominantly from the remote Laurentide and Antarctic ice sheets[49].

Our new account of the EIS collapse is an important step towards solving the mysteries of the Bølling event and the MWP-1a, which also raises a number of research questions pertinent to climate change scenarios for the near future.

(1) What triggered the collapse of the marine-based EIS? In addition to the abrupt atmospheric and surface ocean warming at the Bølling transition[35,50,51], proxy records from core JM02-460 suggest a marked subsurface warming on the Barents Sea continental shelf during the late Heinrich Stadial 1[52], close to the inferred ice sheet grounding line (Fig. 1). A vast ice-ocean interface rendered marine-based EIS sectors potentially very sensitive to subsurface warming and melting at the grounding line, which is considered to be one of the main drivers of current[53,54] and past[55] mass loss from the Antarctic ice sheets.

(2) Which mechanisms drove the rapid EIS retreat? In addition to surface melting and the likely involvement of mass-balance/elevation feedback[41], continuity between subglacially carved lineations and iceberg ploughmarks in the Bear Island Trough suggests calving of deep-keeled icebergs at the ice front[56]. These findings are consistent with the operation of the marine ice cliff instability mechanism (MICI)[57,58] during the rapid ice sheet retreat. The current water depth in the SW Barents Sea is 400-500 m, less than the ~800 m thought to be required by MICI[57]. Isostatic depression by ice sheet loading[59], however, may have lowered the bed sufficiently for this mechanism to operate. Alternatively, the MICI may operate at shallower depths than currently parameterized in models. Although past Antarctic deglaciation events can be explained without invoking this specific mechanism[60], the MICI is featured in the model yielding the high-end future rate of ice loss from the Antarctic Ice Sheet[18].

(3) What was the impact of EIS meltwater on ocean circulation? We estimate that a meltwater flux of 0.2 Sv over 300 yr was injected into the Norwegian Sea and the Arctic Ocean during the early Bølling, a time period when proxy evidence suggests vigorous Atlantic meridional overturning circulation[11,12,61]. This result implies that the relationship between freshwater injection and North Atlantic deep water formation is not clear-cut, and highlights the need to resolve meltwater routing[62].

Our reconstruction of the EIS deglaciation shows that an ice sheet comparable in size to the West Antarctic ice sheet can collapse in as little as 300-500 years. Ice sheet models used to predict the future of marine-based Antarctic ice sheets differ markedly in their predicted rates of ice loss and in the mechanisms involved[17,18]. We provide new empirical constraints that raise the prospect of using the marine-based EIS collapse as a benchmark for validating such ice sheet models and ultimately improve projections of future sea-level rise. The estimated rates of ice loss from the EIS during the early Bølling (~1.6 cm SLE yr^{-1} averaged over 300 yr, peaking at ~2.2 cm SLE yr^{-1}) are comparable to high-end values of mass loss projected for the West Antarctic ice sheet in the next centuries[18].

Methods

Temporal evolution of the marine radiocarbon reservoir age (*R*)

We compiled a time series of 41 new and 58 previously published AMS ^{14}C ages of the polar subsurface-dwelling planktonic foraminifer *Neoglobigerina pachyderma* sinistral, from four Norwegian Sea sediment cores (Fig. 2).

Sediments from core GS07-148-17GC were continously sampled in 0.5 cm thick slices that were dried and washed over 45 and 100 μm sieves. From the >100 μm grain size fraction, 47 samples of monospecific *Neoglobigerina pachyderma* (sinistral) were picked and measured for ^{14}C at the Atmosphere and Ocean Research Institute (AORI) at the University of Tokyo. Foraminiferal tests were weighed and washed ultrasonically before converting them into graphite under the protocol described in[63]. For samples smaller than 0.3 mgC, a specially designed high vacuum line was used for the preparation[64]. Target graphite was then measured by the single stage accelerator mass spectrometer at AORI[65].

The ^{14}C data and other records from three of the cores (MD95-2010, HM79-6 and GIK23074) were previously published[32,34–36]. These cores were stratigraphically aligned to core GS07-148-17GC using tie-points defined by a combination of records of ice rafted detritus (IRD), magnetic susceptibility (MS) and the δ^{18}O and δ^{13}C of *N. pachyderma* sinistral (Supplementary Fig. 5). The alignment to the GS07-148-17GC depth scale was performed with the Oxcal v4.3.2 software[66], using the P_Sequence sediment deposition model[67] and the variable k option[68]. We assume an uncertainty of $\pm$ 2 cm (1σ) for each tie-point.

Absolute age control of the core records including ^{14}C was obtained by event-stratigraphic correlation with the U/Th dated H82 speleothem δ^{18}O record from Hulu Cave, China[28] and isotope records from Greenland Summit ice cores[33] (Supplementary Fig. 1). The rationale for this correlation rests on the close relationship between Greenland temperatures, North Atlantic Ocean temperature and circulation, and the Asian Monsoon on annual to decadal time scales[22–25,27].

For the correlation we used the MS record of core GS07-148-17GC determined in 2 mm steps by a Geotek$^{\text{TM}}$ multi sensor core logger and a Bartington2 point sensor. MS in Norwegian Sea sediments is considered to be a proxy for the strength of the warm Atlantic Water inflow over the basaltic Iceland Scotland Ridge through ocean current erosion and transport of magnetic mineral grains that are subsequently deposited in the S-Norwegian sea; the Atlantic water inflow is in turn tightly linked to the general North Atlantic climate, including Greenland temperatures[32,69–71]. In the Marine Isotope Stage 3 (MIS-3) time interval, the magnetic signal in SE-Norwegian Sea MS records is carried by ferromagnetic low-Ti titanomagnetites sourced from weathered basalt on the Iceland-Scotland ridge[70,71]. To test if this interpretation can be extended into the HS1-Bølling interval we have therefore obtained hysteresis and isothermal remanent magnetization curves of discrete samples using a Kazan University J_Meter coercivity spectrometer at the University of Bergen EarthLab facility. These analyses, combined with semi-quantitative chemical profiles from XRF-core scanning (Supplementary Fig. 2), confirm that the MS signal is driven by the concentration of ferromagnetic minerals, and support the interpretation that these are most likely pseudo single domain low-Ti titanomagnetites derived from weathered basalts of the Iceland-Scotland ridge.

We used the Hulu cave speleothem H82 δ^{18}O record as the Norwegian Sea MS correlation target because of its high temporal resolution, and because it contains high-amplitude signals that covary with the MS record. This covariance has been attributed to fast atmospheric teleconnections operating on annual to decadal timescales between ocean circulation and sea-ice in the North Atlantic and regional Asian monsoon intensity and isotopic fractionation during moisture transport that is captured in the speleothem δ^{18}O[23,27,72]. Experiments with general circulation models suggest that North Atlantic climate and low latitude hydrology are physically linked through the growth of Northern Hemisphere ice cover and amplified Northern Hemisphere cooling, which affects the position of the intertropical convergence zone and the monsoon systems[73–75]. The co-variation between Greenland ice core δ^{18}O and Norwegian sea MS, which is generally very strong at stadial-interstadial transitions[76], is less pronounced during HS1, consistent with the finding that North Atlantic climate was decoupled from Greenland temperatures during cold intervals[77]. The Hulu Cave H82 chronology rests solidly on a large number of U/Th dates that, paired with AMS ^{14}C measurements, yield a high-resolution time series of atmospheric ^{14}C ages[28], which forms the backbone of the IntCal13 atmospheric radiocarbon reconstruction[31]. By tying our Norwegian Sea ^{14}C record directly to the Hulu Cave δ^{18}O, we operate on the same absolute time scale as IntCal13. Hence, we can determine the reservoir age effect in the Norwegian Sea (the difference between the IntCal13 atmospheric ^{14}C ages and the Norwegian Sea ^{14}C ages). This approach is more precise than tying the Norwegian Sea record to the Greenland ice core chronology (GICC05)[78], which has a cumulative counting error of up to $\pm$400 yr in the time interval considered here.

The GS07-148-17GC age model was constructed using the Oxcal v4.3.2 software[66], and the P_Sequence sediment deposition model[67] with the variable k option[68]. The age-uncertainty for each tie-point was derived from a Oxcal P_Sequence model of the H82 speleothem, using the U/Th dates from Ref.[28] (Supplementary Fig. 1). To account for uncertainty in the lead-lag relationships between the records, we assume an added uncertainty of $\pm$ 25 yr (1σ) to each tie-point. Although the correlation depicted in Supplementary Fig. 1 is very detailed, the resulting age-depth relationship for the Norwegian Sea cores remains smooth and roughly linear between the Holocene boundary and an interval of rapid deposition centered at 17.5 ka that is related to the break-up of the Norwegian Channel Ice Stream[79,80] and a catastrophic drainage of a large ice dammed lake in the North Sea[81]. Our correlation is validated by the occurrence of the Vedde Ash layer in the interval ascribed to Younger Dryas both in the GS07-148-17GC and in the Greenland ice core records[33] (Supplementary Fig. 1).

To assess the sensitivity of our results to the reconstructed chronology, we explored an alternative deposition model without any assumptions of teleconnections or synchrony between proxy records (Supplementary Fig. 3). We constrained the ages of this alternative model with the Vedde Ash, which is dated by layer counting in the Greenland ice cores to 12121 $\pm$ 57 cal yr BP on the GICC05 chronology[82] (Supplementary Fig. 1), and with 24 ^{14}C dates from our compilation (Supplementary data file). We restricted the use of ^{14}C dates to the Younger Dryas and Bølling-Allerød time periods where the Norwegian Sea R has been independently constrained by paired marine and terrestrial ^{14}C dates[30]. We then used the *Marine13* calibration curve[31] with a ΔR of 100 $\pm$ 50 yr, and the same deposition model as in our preferred chronology, invoking the default *general* outlier model[83]. Due to a lack of pre-Bølling age constraints, this alternative chronology expectedly shows much greater pre-Bølling age uncertainty than our preferred chronology. Nevertheless, the two chronologies overlap almost entirely in their 68.2 % (1σ) credible intervals (Supplementary Fig. 3). Notably, the alternative chronology yields a drop in ^{14}C age at the Bølling transition that is steeper than in our preferred chronology, implying an even more abrupt EIS collapse. Hence, we conclude that the inferred drop in R at the Bølling transition is unlikely to be an artefact of the age model, and that our estimates are conservative in terms of the rate of EIS mass loss and its contribution to the MWP-1a.

From the compiled time series of ^{14}C ages we calculate R as the difference between the Norwegian Sea ^{14}C and the *Intcal13* atmospheric ^{14}C calibration curve[31] (Fig. 2F). To incorporate the uncertainty in both calendar ages and ^{14}C ages in our reconstructed ^{14}C and R record, we generated an uncertainty envelope by Monte Carlo sampling of multiple posterior probability density functions (PDFs) generated by the Oxcal sediment deposition models of the core stratigraphies: (i) PDFs of the stratigraphic alignment of the four Norwegian Sea sediment cores, (ii) PDFs of the depositional model for the GS07-148-17GC core, which incorporate both the uncertainty in the Hulu Cave target δ^{18}O record and uncertainty in the correlation to the Hulu Cave record, and (iii) PDFs of the ^{14}C measurements. Our time series of ^{14}C ages is the mean $\pm$ 1σ of 10^5 Monte Carlo realizations of the dataset in 10-yr bins using linear interpolation. It spans the period from 12,200 to 19,000 cal yr BP and is available as supplementary data formatted as a .14c file that can be used directly in radiocarbon calibration software.

Our R record are consistent with R values previously reported from the North Atlantic and the Norwegian Sea and coast[30,36,84–86]. Although a different approach was used to constrain the calender ages of core GIK23074[36], we arrive at similar reservoir ages.

Tephrochonology

Tephra shards were quantified in the >100 μm grain fraction in ~20 cm interval of core GS07-148-17GC corresponding to the Younger Dryas chronozone. This interval was chosen with the aim of finding the Vedde Ash tephra that is a key chronostratigraphic marker horizon in the North Atlantic region, and is also found in the Greenland Ice cores[33] and several of the Norwegian Sea cores used in this study[32,35]. Based on their colour and morphological character, tephra particles were grouped into a transparent-white rhyolitic type of tephra and a brown basaltic type of tephra. The total count from each of these tephra types was normalized using the total dry weight of the samples and the results plotted versus depth (Supplementary Fig. 1)

Tephra shards from three depth intervals (32.5-33.0, 33.5-34.0 and 36.0-36.5 cm) were selected for geochemical analysis. 25-30 shards of both rhyolitic and basaltic type were picked for major oxide geochemical analysis on the University of Bergen Zeiss Supra 55 VP scanning electron microscope. The microscope was attached to a Thermo energy dispersive X-ray spectrometer with 9.5 mm working distance, beam current of 1.00 mA, an aperture size of 60 μm, beam width of 6 μm and detection time of 60 s. The results are presented in the Supplementary Data File and in Supplementary Fig. 4. As the geochemical analysis were performed directly on the shards and without any leveling or polishing the beam will hit the surface from different angles. This resulted in that the counting rate of the different elements becomes slightly more scattered than during analysis on a polished thin section. The major element composition is, however, consistent with published major element data from the Vedde Ash (Supplementary Fig. 4).

Ice sheet margin reconstructions

We reconstructed the deglaciation of the EIS complex in a Bayesian chronological framework using Oxcal 4.2.4[66–68,83]. The prior model was constructed using available chronological, stratigraphical and morphological data that were aggregated, independently for the BSIS and the FIS, into a sequence of phases with known relative ages. A phase in this context refers to the retreat (or advance) of the ice sheet in a specific area.

We grouped the deglaciation of the FIS ice sheet into two phases: (i) late HS1 advance and (ii) deglaciation on the continental shelf and outer coasts. Following the deglaciation of the continental shelf, we use the ages and ice sheet geometries provided by the *Dated-1* reconstruction[19] in the 14-10 ka interval, as these are predominantly based on terrestrial dates not affected by our recalibration of the marine ^{14}C dates. The ice margins along the southern and eastern margins of the FIS were generated by interpolating between the 15 ka and 14 ka *Dated-1* ice margins using the TopoToRaster tool in ArcMap 10.5.1. On the Norwegian continental shelf, evidence suggests that the deeper troughs deglaciated rapidly compared to the shallower banks[87–89].

The more complex deglaciation history of the BSIS was divided into five phases: (i) late HS1 advance, (ii) deglaciation of the major overdeepened areas of Storfjorden trough, Bear Island trough and Franz Victoria trough, and the narrow continental shelf areas west and north of Svalbard, (iii) deglaciation of the Central Deep, (iv) final deglaciation of the shallow banks in the northern Barents Sea, and (v) ice retreat to the Svalbard archipelago. An early deglacial phase was added before the late HS1 advance, without assigning ice sheet margins. At 12-10 ka we used the *Dated-1*[19] BSIS ice sheet geometries.

We adapt a previously proposed ice sheet retreat pattern for the southern Barents Sea, suggesting episodic rapid retreat in the Bear Island trough[90–94]. Well preserved retreat ridges suggest that the ice remaining on the shallower banks retreated more slowly[92]. The final ice movement on the southern Barents sea banks was from the east[92,94] suggesting an ice dome remained over the Central Deep following the separation of the BSIS and the FIS (Fig. 1).

The age-control of each phase was constrained by the ages of sediment facies and/or facies transitions linked to ice margin positions within the phase (Supplementary Figs. 8 and 9), as well as by the age information of adjacent phases in the sequence. We used the published ^{14}C dates either directly as ages of the sampled sedimentary units, or, in cases where sufficient published dates and stratigraphic information were available, used PDFs of sediment unit boundaries (e.g. the boundary between subglacial till and glacial-proximal sedimentary facies) generated with the OxCal P_Sequence deposition model[67,68]. Outliers were detected and dealt with using the default *general* outlier model in Oxcal[83] (Supplementary Figs. 8;9). To account for possible deviations in R from the reconstructed Norwegian Sea ^{14}C and Marine13, we add a ΔR of 0 ± 50 ^{14}C years ($1\ \sigma$) to each marine radiocarbon age determination. To calibrate marine conventional ^{14}C ages younger than 11800 ^{14}C years, we use the Marine13 curve[31], terrestrial dates are calibrated with the IntCal13[31].

For each phase of the deglaciation we outlined a succession of ice margins (Fig. 1) based on published sediment core data, geomorphological interpretations and ice sheet reconstructions for the BSIS[19,21,52,90–129] and FIS[19,45,51,80,81,87–89,118,130–143]. The available information is, however, too sparse to yield continuous time-synchronous margins and we stress that the reconstructed margins are intended to capture the general pattern of retreat rather that to be accurate representation of the ice sheet at a specific time. To account for uncertainty in the ice sheet geometry, we follow the approach of[19] and construct accompanying maximum and minimum margins (Fig. 1). These are treated as the 95% quantiles. For margins derived from the *Dated-1* reconstruction, we use the their max and min margins[19].

Ice sheet volume estimates

We converted the reconstructed ice sheet areas to volumes using the approximation proposed by Paterson[39]: $\log V = 1.23(\log S - 1)$, where V is volume and S is area. Paterson's formula was determined empirically by regression of measurements on six extant ice sheets and ice caps, the boundary conditions of which are not directly comparable to those of the EIS. To assess the sensitivity of the volume estimates to the regression assumptions, we also used the area-volume relationships from the output of a recent ice-sheet model of the EIS[40] to convert the reconstructed areas volume (Supplementary Fig. 10). Although the model-based regression yields an EIS volume that is 2.7 m SLE smaller than the Paterson approximation at the start of the deglaciation, the difference in the estimated ice loss between 14.7 and 14.4 kyr BP is only ~0.2 m SLE, which is negligible with respect to our conclusions (Supplementary Fig. 10). Paleo-depths of the continental shelves on which the EIS was grounded are obscured by an unknown amount of isostatic uplift since deglaciation. Without correcting for ice volume below flotation through glacio-isostatic modelling, which is outside the scope of our study, our estimated volumes cannot be interpreted as eustatic sea-level change. For each ice sheet margin reconstruction and associated uncertainty estimates, we generated a PDF of the volume estimate using Gaussian kernels. The volume-PDF and accompanying age-PDF of each reconstructed ice sheet were resampled using a Monte Carlo technique detailed at https://github.com/kahaaga/EurasianDeglaciation.

The effect of bioturbation

The Norwegian Sea sediment core GS07-148-17GC (Fig. 1) features a large, complex burrow with open cavities containing pellets (Supplementary Fig. 6). Unlike ambient biogenic sediment mixing, which is typically limited to an upper mixed layer, this burrow (or set of burrows) extends ~25 cm down into the late HS1, and may have transported younger material down through this stratigraphic interval. Seven ^{14}C dates from this interval of the GS07-148-17GC core deviate from the ages in nearby cores GIK23074 and HM79-6 (Fig. 1) at the same stratigraphic level. The presence of the large burrow through this interval compelled us to discard these ^{14}C dates from the ^{14}C reconstruction (Supplementary Fig. 5).

To assess the potential impact of ambient biogenic sediment mixing on the observed decline in R at the Bølling transition, we used the TURBO2 model[144], a mixed layer model with instantaneous mixing designed to simulate the effects of bioturbation on proxy records from sedimentary particles such as foraminifera. As input we used 1,024 simulated vectors of abundance generated as normally distributed random values centered on the best-fit linear trend and with the standard deviation of the observed record of the abundance of foraminifera from the MD95-2010 core[32]. The simulated number of specimens picked for measurement was set to 200. To focus on the change in R across the Bølling transition, we limited the modeling to the time interval between ~15,400 and ~13,700 calendar yr BP. To keep the model as simple as possible, we let the hypothetical true decline in R be an instantaneous step change superimposed on the overall linear trend in the observed ^{14}C record, and we assumed a constant mixed layer depth. Under this scenario, if we invoked a drop in the modeled R record of ~1,220 ^{14}C yr from 14,600 to 14,550 calendar yr BP and used a mixed layer depth of 6 cm, then the bioturbated ^{14}C ages simulated by TURBO2 provided a reasonable fit to the observed ^{14}C record (Supplementary Fig. 7). Hence, the effect of bioturbation would be to temporally smear out a more abrupt event in the ^{14}C record. This smearing effect pushes the recalibrated ^{14}C ages for the start of the deglaciation backwards in time, and attenuates the estimated EIS melt water flux. An upward bias towards older ages affects ^{14}C dates between ~13,200 and 14,000 ^{14}C yr BP in particular, and is important to bear in mind if the ^{14}C record is to be used as a regional calibration curve.

Acknowledgements

This work is funded by the Research Council of Norway trough grants no. 221999 (JB) and 231259 (BH), and by the Bergen Research Foundation (BH). JB was also supported through the RISES project of the Centre for Climate Dynamics at the Bjerknes Centre for Climate Research. Additional support was received from JSPS KAKENHI 17H01168 and 15KK0151 (YY). JB, HH, KAH and BH acknowledge discussions with colleagues at the department of Earth Science and the Bjerknes Centre for Climate Research at the University of Bergen. We thank the captain and crew of R/V G.O. Sars for retrieving Core GS07-148-17GC. Harald Walderhaug is thanked for help with, and discussions around the paleomagnetic analyses. Salad Yusuf Ali, Kristin Flesland and Eivind N. Støren is thanked for technical support.

Author contributions

J.B. conceived and designed the study, developed the core chronology, the deglaciation chronology, and the ice margin reconstruction. H.H. collected sediment core GS07-148-17GC and performed tephrochronological and geochemical analyses. Y. Y. performed AMS ^{14}C analyses. K. A. H. and J.B. developed the Norwegian Sea ^{14}C reconstruction and performed statistical analyses. B. H. performed bioturbation modelling. J.B., B.H. and K. A. H. wrote the paper, and all authors contributed to the writing of the final version of the manuscript.

References

[1] Stocker, T. *Climate change 2013: the physical science basis: Working Group I contribution to the Fifth assessment report of the Intergovernmental Panel on Climate Change* (Cambridge University Press, 2014).

[2] Fairbanks, R. G. A 17,000-year glacio-eustatic sea level record: influence of glacial melting rates on the Younger Dryas event and deep-ocean circulation. *Nature* **342**, 637–642 (1989).

[3] Blanchon, P. & Shaw, J. Reef drowning during the last deglaciation: Evidence for catastrophic sea-level rise and ice-sheet collapse. *Geology* **23**, 4 (1995). URL +http://dx.doi.org/10.1130/0091-7613(1995)023{%}3C0004:RDDTLD{%}3E2.3.CO;2.

[4] Hanebuth, T., Stattegger, K. & Grootes, P. M. Rapid flooding of the Sunda Shelf: a late-glacial sea-level record. *Science* **288**, 1033–1035 (2000).

[5] Deschamps, P. *et al.* Ice-sheet collapse and sea-level rise at the Bølling warming 14,600 years ago. *Nature* **483**, 559–564 (2012).

[6] Liu, J., Milne, G. A., Kopp, R. E., Clark, P. U. & Shennan, I. Sea-level constraints on the amplitude and source distribution of Meltwater Pulse 1A. *Nature Geoscience* **9**, 130 (2016).

[7] Bassett, S. E., Milne, G. A., Mitrovica, J. X. & Clark, P. U. Ice sheet and solid earth influences on far-field sea-level histories. *Science* **309**, 925–928 (2005).

[8] Clark, P. U. *et al.* Origin of the first global meltwater pulse following the last glacial maximum. *Paleoceanography* **11**, 563–577 (1996).

[9] Clark, P. U., Mitrovica, J. X., Milne, G. A. & Tamisiea, M. E. Sea-level fingerprinting as a direct test for the source of global meltwater pulse IA. *Science* **295**, 2438–2441 (2002).

[10] Carlson, A. E. & Clark, P. U. Ice sheet sources of sea level rise and freshwater discharge during the last deglaciation. *Reviews of Geophysics* **50** (2012). URL https://agupubs.onlinelibrary.wiley.com/doi/abs/10.1029/2011RG000371.

[11] McManus, J. F., Francois, R., Gherardi, J.-M., Keigwin, L. D. & Brown-Leger, S. Collapse and rapid resumption of Atlantic meridional circulation linked to deglacial climate changes. *Nature* **428**, 834 (2004).

[12] Stanford, J. D., Rohling, E. J., Bacon, S. & Holliday, N. P. A review of the deep and surface currents around Eirik Drift, south of Greenland: Comparison of the past with the present. *Global and Planetary Change* **79**, 244–254 (2011).

[13] Weertman, J. Stability of the junction of an ice sheet and an ice shelf. *Journal of Glaciology* **13**, 3–11 (1974).

[14] Mercer, J. H. West Antarctic ice sheet and CO2 greenhouse effect: a threat of disaster. *Nature* **271**, 321 (1978).

[15] Hughes, T. J. The weak underbelly of the West Antarctic ice sheet. *Journal of Glaciology* **27**, 518–525 (1981).

[16] Joughin, I., Smith, B. E. & Medley, B. Marine ice sheet collapse potentially under way for the Thwaites Glacier Basin, West Antarctica. *Science* **344**, 735–738 (2014).

[17] Ritz, C. *et al.* Potential sea-level rise from Antarctic ice-sheet instability constrained by observations. *Nature* **528**, 115 (2015).

[18] DeConto, R. M. & Pollard, D. Contribution of Antarctica to past and future sea-level rise. *Nature* **531**, 591 (2016).

[19] Hughes, A. L. C., Gyllencreutz, R., Lohne, Ø. S., Mangerud, J. & Svendsen, J. I. The last Eurasian ice sheets – a chronological database and time-slice reconstruction, DATED-1. *Boreas* **45**, 1–45 (2016). URL http://dx.doi.org/10.1111/bor.12142.

[20] Stouffer, R. J. *et al.* Investigating the causes of the response of the thermohaline circulation to past and future climate changes. *Journal of Climate* **19**, 1365–1387 (2006).

[21] Hormes, A., Gjermundsen, E. F. & Rasmussen, T. L. From mountain top to the deep sea–Deglaciation in 4D of the northwestern Barents Sea ice sheet. *Quaternary Science Reviews* **75**, 78–99 (2013).

[22] Wang, Y. J. *et al.* A High-Resolution Absolute-Dated Late Pleistocene Monsoon Record from Hulu Cave, China. *Science* **294**, 2345–2348 (2001). URL http://science.sciencemag.org/content/294/5550/2345.

[23] Orland, I. J. *et al.* Direct measurements of deglacial monsoon strength in a Chinese stalagmite. *Geology* **43**, 555 (2015). URL +http://dx.doi.org/10.1130/G36612.1.

[24] Cheng, H. *et al.* Ice Age Terminations. *Science* **326**, 248–252 (2009). URL http://science.sciencemag.org/content/326/5950/248.

[25] Deplazes, G. *et al.* Links between tropical rainfall and North Atlantic climate during the last glacial period. *Nature Geoscience* **6**, 213 (2013).

[26] Hughen, K., Southon, J., Lehman, S., Bertrand, C. & Turnbull, J. Marine-derived ^{14}C calibration and activity record for the past 50,000 years updated from the Cariaco Basin. *Quaternary Science Reviews* **25**, 3216–3227 (2006).

[27] Liu, Y. H. *et al.* Links between the East Asian monsoon and North Atlantic climate during the 8,200 year event. *Nature Geoscience* **6**, 117 (2013).

[28] Southon, J., Noronha, A. L., Cheng, H., Edwards, R. L. & Wang, Y. A high-resolution record of atmospheric ^{14}C based on Hulu Cave speleothem H82. *Quaternary Science Reviews* **33**, 32–41 (2012).

[29] Wu, J., Wang, Y., Cheng, H. & Edwards, L. R. An exceptionally strengthened East Asian summer monsoon event between 19.9 and 17.1 ka BP recorded in a Hulu stalagmite. *Science in China Series D: Earth Sciences* **52**, 360–368 (2009). URL https://doi.org/10.1007/s11430-009-0031-1.

[30] Bondevik, S., Mangerud, J., Birks, H. H., Gulliksen, S. & Reimer, P. Changes in North Atlantic radiocarbon reservoir ages during the Allerød and Younger Dryas. *Science* **312**, 1514–1517 (2006).

[31] Reimer, P. J. *et al.* IntCal13 and Marine13 radiocarbon age calibration curves 0–50,000 years cal BP. *Radiocarbon* **55**, 1869–1887 (2013).

[32] Dokken, T. M. & Jansen, E. Rapid changes in the mechanism of ocean convection during the last glacial period. *Nature* **401**, 458–461 (1999).

[33] Seierstad, I. K. *et al.* Consistently dated records from the Greenland GRIP, GISP2 and NGRIP ice cores for the past 104ka reveal regional millennial-scale δ^{18}O gradients with possible Heinrich event imprint. *Quaternary Science Reviews* **106**, 29–46 (2014). URL http://www.sciencedirect.com/science/article/pii/S027737911400434X.

[34] Voelker, A. H. L. *Zur Deutung der Dansgaard-Oeschger Ereignisse in ultra-hochauflösenden Sedimentprofilen aus dem Europäischen Nordmeer*. Ph.D. thesis, Institut für Geowissenschaften, Christian-Albrechts-Universität (1999).

[35] Karpuz, N. K. & Jansen, E. A high-resolution diatom record of the last deglaciation from the SE Norwegian Sea: Documentation of rapid climatic changes. *Paleoceanography* **7**, 499–520 (1992). URL http://dx.doi.org/10.1029/92PA01651.

[36] Sarnthein, M., Balmer, S., Grootes, P. M. & Mudelsee, M. Planktic and benthic ^{14}C reservoir ages for three ocean basins, calibrated by a suite of ^{14}C plateaus in the glacial-to-deglacial Suigetsu atmospheric ^{14}C record. *Radiocarbon* **57**, 129–151 (2015).

[37] Dreger, D. *Decadal to Centennial Scale Sediment Records of Ice Advance on the Barents Shelf and Meltwater Discharge Into the Northeastern Norwegian Sea Over the Last 40 Kyr: Dekadische Bis Jahrhundert-Variabilität Von Eisvorstößen Auf Dem Barentsschelf und Schmelzwasserschüben in Die Nordöstliche Norwegensee Während Der Letzten 40 Ka*. Ph.D. thesis, Inst. für Geowiss. (1999).

[38] Sarnthein, M. *et al.* Fundamental modes and abrupt changes in North Atlantic circulation and climate over the last 60 ky—Concepts, reconstruction and numerical modeling. In *The Northern North Atlantic*, 365–410 (Springer, 2001).

[39] Paterson, W. S. B. Laurentide Ice Sheet: estimated volumes during late Wisconsin. *Reviews of Geophysics* **10**, 885–917 (1972).

[40] Patton, H. *et al.* Deglaciation of the Eurasian ice sheet complex. *Quaternary Science Reviews* **169**, 148–172 (2017). URL http://www.sciencedirect.com/science/article/pii/S0277379117302068.

[41] Gregoire, L. J., Otto-Bliesner, B., Valdes, P. J. & Ivanovic, R. Abrupt Bølling warming and ice saddle collapse contributions to the Meltwater Pulse 1a rapid sea level rise. *Geophysical research letters* **43**, 9130–9137 (2016).

[42] Tarasov, L., Dyke, A. S., Neal, R. M. & Peltier, W. R. A data-calibrated distribution of deglacial chronologies for the North American ice complex from glaciological modeling. *Earth and Planetary Science Letters* **315**, 30–40 (2012).

[43] Bentley, M. J. *et al.* A community-based geological reconstruction of Antarctic Ice Sheet deglaciation since the Last Glacial Maximum. *Quaternary Science Reviews* **100**, 1–9 (2014).

[44] Gomez, N., Mitrovica, J. X., Tamisiea, M. E. & Clark, P. U. A new projection of sea level change in response to collapse of marine sectors of the Antarctic Ice Sheet. *Geophysical Journal International* **180**, 623–634 (2010).

[45] Romundset, A., Bondevik, S. & Bennike, O. Postglacial uplift and relative sea level changes in Finnmark, northern Norway. *Quaternary Science Reviews* **30**, 2398–2421 (2011).

[46] Svendsen, J. I. & Mangerud, J. Late Weichselian and Holocene sea-level history for a cross-section of western Norway. *Journal of Quaternary Science* **2**, 113–132 (1987).

[47] Lohne, Ø. S., Bondevik, S., Mangerud, J. & Svendsen, J. I. Sea-level fluctuations imply that the Younger Dryas ice-sheet expansion in western Norway commenced during the Allerød. *Quaternary Science Reviews* **26**, 2128–2151 (2007).

[48] Vasskog, K. *et al.* Evidence of early deglaciation (18 000 cal a bp) and a postglacial relative sea-level curve from southern Karmøy, south-west Norway. *Journal of Quaternary Science* (2019).

[49] Shennan, I. *et al.* Relative sea-level changes, glacial isostatic modelling and ice-sheet reconstructions from the British Isles since the Last Glacial Maximum. *Journal of Quaternary Science: Published for the Quaternary Research Association* **21**, 585–599 (2006).

[50] Buizert, C. *et al.* Greenland temperature response to climate forcing during the last deglaciation. *Science* **345**, 1177–1180 (2014).

[51] Haflidason, H., Sejrup, H. P., Kristensen, D. K. & Johnsen, S. Coupled response of the late glacial climatic shifts of northwest Europe reflected in Greenland ice cores: Evidence from the northern North Sea. *Geology* **23**, 1059–1062 (1995).

[52] Rasmussen, T. L. *et al.* Paleoceanographic evolution of the SW Svalbard margin (76 N) since 20,000 ^{14}C yr BP. *Quaternary Research* **67**, 100–114 (2007).

[53] Jenkins, A. *et al.* Observations beneath Pine Island Glacier in West Antarctica and implications for its retreat. *Nature Geoscience* **3**, 468 (2010).

[54] Jacobs, S. S., Jenkins, A., Giulivi, C. F. & Dutrieux, P. Stronger ocean circulation and increased melting under Pine Island Glacier ice shelf. *Nature Geoscience* **4**, 519 (2011).

[55] Yokoyama, Y. *et al.* Widespread collapse of the Ross Ice Shelf during the late Holocene. *Proceedings of the National Academy of Sciences* **113**, 2354–2359 (2016).

[56] Piasecka, E. D., Stokes, C. R., Winsborrow, M. C. M. & Andreassen, K. Relationship between mega-scale glacial lineations and iceberg ploughmarks on the Bjørnøyrenna Palaeo-Ice Stream bed, Barents Sea. *Marine Geology* **402**, 153–164 (2018).

[57] Pollard, D., DeConto, R. M. & Alley, R. B. Potential Antarctic Ice Sheet retreat driven by hydrofracturing and ice cliff failure. *Earth and Planetary Science Letters* **412**, 112–121 (2015).

[58] Wise, M. G., Dowdeswell, J. A., Jakobsson, M. & Larter, R. D. Evidence of marine ice-cliff instability in Pine Island Bay from iceberg-keel plough marks. *Nature* **550**, 506 (2017).

[59] Howell, D., Siegert, M. J. & Dowdeswell, J. A. Modelling the influence of glacial isostasy on Late Weichselian ice-sheet growth in the Barents Sea. *Journal of Quaternary Science: Published for the Quaternary Research Association* **15**, 475–486 (2000).

[60] Edwards, T. L. *et al.* Revisiting Antarctic ice loss due to marine ice-cliff instability. *Nature* **566**, 58 (2019).

[61] Ng, H. C. *et al.* Coherent deglacial changes in western Atlantic Ocean circulation. *Nature communications* **9** (2018).

[62] Condron, A. & Winsor, P. Meltwater routing and the Younger Dryas. *Proceedings of the National Academy of Sciences* **109**, 19928–19933 (2012).

[63] Yokoyama, Y., Miyairi, Y., Matsuzaki, H. & Tsunomori, F. Relation between acid dissolution time in the vacuum test tube and time required for graphitization for AMS target preparation. *Nuclear Instruments and Methods in Physics Research Section B: Beam Interactions with Materials and Atoms* **259**, 330–334 (2007).

[64] Yokoyama, Y., Koizumi, M., Matsuzaki, H., Miyairi, Y. & Ohkouchi, N. Developing ultra small-scale radiocarbon sample measurement at the University of Tokyo. *Radiocarbon* **52**, 310–318 (2010).

[65] Yokoyama, Y. *et al.* A Single Stage Accelerator Mass Spectrometry at the Atmosphere and Ocean Research Institute, The University of Tokyo. *Nuclear Instruments and Methods in Physics Research Section B* (2018).

[66] Bronk Ramsey, C. Bayesian analysis of radiocarbon dates. *Radiocarbon* **51**, 337–360 (2009).

[67] Bronk Ramsey, C. Deposition models for chronological records. *Quaternary Science Reviews* **27**, 42–60 (2008).

[68] Bronk Ramsey, C. & Lee, S. Recent and planned developments of the program OxCal. *Radiocarbon* **55**, 720–730 (2013).

[69] Rasmussen, T. L., van Weering, T. C. E. & Labeyrie, L. Climatic instability, ice sheets and ocean dynamics at high northern latitudes during the last glacial period (58-10 KA BP). *Quaternary Science Reviews* **16**, 71–80 (1997). URL http://www.sciencedirect.com/science/article/pii/S0277379196000455.

[70] Kissel, C. *et al.* Rapid climatic variations during marine isotopic stage 3: magnetic analysis of sediments from Nordic Seas and North Atlantic. *Earth and Planetary Science Letters* **171**, 489–502 (1999). URL http://www.sciencedirect.com/science/article/pii/S0012821X99001624.

[71] Ballini, M., Kissel, C., Colin, C. & Richter, T. Deep-water mass source and dynamic associated with rapid climatic variations during the last glacial stage in the North Atlantic: A multiproxy investigation of the detrital fraction of deep-sea sediments. *Geochemistry, Geophysics, Geosystems* **7**, n/a—-n/a (2006). URL http://dx.doi.org/10.1029/2005GC001070.

[72] Liu, Z. *et al.* Chinese cave records and the East Asia summer monsoon. *Quaternary Science Reviews* **83**, 115–128 (2014).

[73] Chiang, J. C. H. & Bitz, C. M. Influence of high latitude ice cover on the marine Intertropical Convergence Zone. *Climate Dynamics* **25**, 477–496 (2005).

[74] Broccoli, A. J., Dahl, K. A. & Stouffer, R. J. Response of the ITCZ to Northern Hemisphere cooling. *Geophysical Research Letters* **33** (2006).

[75] Pausata, F. S. R., Battisti, D. S., Nisancioglu, K. H. & Bitz, C. M. Chinese stalagmite δ^{18}O controlled by changes in the Indian monsoon during a simulated Heinrich event. *Nature Geoscience* **4**, 474 (2011).

[76] Sadatzki, H. *et al.* Sea ice variability in the southern Norwegian Sea during glacial Dansgaard-Oeschger climate cycles. *Science advances* **5**, eaau6174 (2019).

[77] Landais, A. *et al.* Ice core evidence for decoupling between midlatitude atmospheric water cycle and Greenland temperature during the last deglaciation. *Climate of the Past* **14**, 1405–1415 (2018).

[78] Andersen, K. K. *et al.* The Greenland ice core chronology 2005, 15–42 ka. Part 1: constructing the time scale. *Quaternary Science Reviews* **25**, 3246–3257 (2006).

[79] Hjelstuen, B. O. *et al.* Late Quaternary seismic stratigraphy and geological development of the south Vøring margin, Norwegian Sea. *Quaternary Science Reviews* **23**, 1847–1865 (2004).

[80] Lekens, W. A. H. *et al.* Laminated sediments preceding Heinrich event 1 in the Northern North Sea and Southern Norwegian Sea: Origin, processes and regional linkage. *Marine Geology* **216**, 27–50 (2005). URL http://www.sciencedirect.com/science/article/pii/S0025322704003585.

[81] Hjelstuen, B. O., Sejrup, H. P., Valvik, E. & Becker, L. W. M. Evidence of an ice-dammed lake outburst in the North Sea during the last deglaciation. *Marine Geology* (2017).

[82] Rasmussen, S. O. *et al.* A new Greenland ice core chronology for the last glacial termination. *Journal of Geophysical Research: Atmospheres* **111** (2006).

[83] Bronk Ramsey, C. Dealing with outliers and offsets in radiocarbon dating. *Radiocarbon* **51**, 1023–1045 (2009).

[84] Waelbroeck, C. *et al.* The timing of the last deglaciation in North Atlantic climate records. *Nature* **412**, 724–727 (2001).

[85] Thornalley, D. J. R., McCave, I. N. & Elderfield, H. Tephra in deglacial ocean sediments south of Iceland: Stratigraphy, geochemistry and oceanic reservoir ages. *Journal of Quaternary Science* **26**, 190–198 (2011). URL http://dx.doi.org/10.1002/jqs.1442.

[86] Stanford, J. D. *et al.* A new concept for the paleoceanographic evolution of Heinrich event 1 in the North Atlantic. *Quaternary Science Reviews* **30**, 1047–1066 (2011). URL http://www.sciencedirect.com/science/article/pii/S0277379111000400.

[87] Dowdeswell, J. A., Ottesen, D., Evans, J., Cofaigh, C. Ó. & Anderson, J. B. Submarine glacial landforms and rates of ice-stream collapse. *Geology* **36**, 819 (2008). URL +http://dx.doi.org/10.1130/G24808A.1.

[88] Rydningen, T. A., Vorren, T. O., Laberg, J. S. & Kolstad, V. The marine-based NW Fennoscandian ice sheet: glacial and deglacial dynamics as reconstructed from submarine landforms. *Quaternary Science Reviews* **68**, 126–141 (2013). URL http://www.sciencedirect.com/science/article/pii/S027737911300067X.

[89] Brendryen, J. *et al.* Ice sheet dynamics on the Lofoten–Vesterålen shelf, north Norway, from Late MIS-3 to Heinrich Stadial 1. *Quaternary Science Reviews* **119**, 136–156 (2015). URL http://www.sciencedirect.com/science/article/pii/S0277379115001225.

[90] Winsborrow, M. C. M., Andreassen, K., Corner, G. D. & Laberg, J. S. Deglaciation of a marine-based ice sheet: Late Weichselian palaeo-ice dynamics and retreat in the southern Barents Sea reconstructed from onshore and offshore glacial geomorphology. *Quaternary Science Reviews* **29**, 424–442 (2010). URL http://www.sciencedirect.com/science/article/pii/S0277379109003333.

[91] Andreassen, K., Winsborrow, M. C. M., Bjarnadóttir, L. R. & Rüther, D. C. Ice stream retreat dynamics inferred from an assemblage of landforms in the northern Barents Sea. *Quaternary Science Reviews* **92**, 246–257 (2014).

[92] Bjarnadóttir, L. R., Winsborrow, M. C. M. & Andreassen, K. Deglaciation of the central Barents Sea. *Quaternary Science Reviews* **92**, 208–226 (2014). URL http://www.sciencedirect.com/science/article/pii/S027737911300348X.

[93] Bjarnadóttir, L. R., Winsborrow, M. C. M. & Andreassen, K. Large subglacial meltwater features in the central Barents Sea. *Geology* **45**, 159 (2017). URL http://dx.doi.org/10.1130/G38195.1.

[94] Newton, A. M. W. & Huuse, M. Glacial geomorphology of the central Barents Sea: Implications for the dynamic deglaciation of the Barents Sea Ice Sheet. *Marine Geology* **387**, 114–131 (2017). URL http://www.sciencedirect.com/science/article/pii/S0025322716302614.

[95] Andreassen, K., Laberg, J. S. & Vorren, T. O. Seafloor geomorphology of the SW Barents Sea and its glaci-dynamic implications. *Geomorphology* **97**, 157–177 (2008). URL http://www.sciencedirect.com/science/article/pii/S0169555X07002917.

[96] Andreassen, K., Bjarnadóttir, L. R., Rüther, D. C. & Winsborrow, M. C. M. Retreat patterns and dynamics of the former Bear Island Trough Ice Stream. *Geological Society, London, Memoirs* **46**, 445–452 (2016). URL http://mem.lyellcollection.org/content/46/1/445.

[97] Bartels, M. *et al.* Atlantic Water advection vs. glacier dynamics in northern Spitsbergen since early deglaciation. *Climate of the Past* **13**, 1717–1749 (2017). URL https://www.clim-past.net/13/1717/2017/.

[98] Bjarnadóttir, L. R. & Andreassen, K. Ice-stream landform assemblage in Kveithola, western Barents Sea margin. *Geological Society, London, Memoirs* **46**, 325–328 (2016). URL http://mem.lyellcollection.org/content/46/1/325.

[99] Bjarnadóttir, L. R., Rüther, D. C., Winsborrow, M. C. M. & Andreassen, K. Grounding-line dynamics during the last deglaciation of Kveithola, W Barents Sea, as revealed by seabed geomorphology and shallow seismic stratigraphy. *Boreas* **42**, 84–107 (2013). URL http://dx.doi.org/10.1111/j.1502-3885.2012.00273.x.

[100] Bondevik, S., Mangerud, J., Ronnert, L. & Salvigsen, O. Postglacial sea-level history of Edgeøya and Barentsøya, eastern Svalbard. *Polar Research* **14**, 153–180 (1995).

[101] Cadman, V. M. *Glacimarine sedimentation and environments during Late Weichselian and Holocene in the Bellsund Trough and Van Keulenfjorden, Svalbard.* Ph.D. thesis, University of Cambridge (1996).

[102] Esteves, M., Bjarnadóttir, L. R., Winsborrow, M. C. M., Shackleton, C. S. & Andreassen, K. Retreat patterns and dynamics of the Sentralbankrenna glacial system, central Barents Sea. *Quaternary Science Reviews* **169**, 131–147 (2017). URL http://www.sciencedirect.com/science/article/pii/S0277379117300550.

[103] Hald, M., Danielsen, T. K. & Lorentzen, S. Late Pleistocene-Holocene benthic foraminiferal distribution in the southwestern Barents Sea: Paleoenvironmental implications. *Boreas* **18**, 367–388 (1989).

[104] Hald, M. *et al.* Late-glacial and Holocene paleoceanography and sedimentary environments in the St. Anna Trough, Eurasian Arctic Ocean margin. *Palaeogeography, Palaeoclimatology, Palaeoecology* **146**, 229–249 (1999).

[105] Hogan, K. A. *et al.* Submarine landforms and ice-sheet flow in the Kvitøya Trough, northwestern Barents Sea. *Quaternary Science Reviews* **29**, 3545–3562 (2010).

[106] Hogan, K. A. *et al.* Subglacial sediment pathways and deglacial chronology of the northern Barents Sea Ice Sheet. *Boreas* **46**, 750–771 (2017). URL http://dx.doi.org/10.1111/bor.12248.

[107] Jessen, S. P., Rasmussen, T. L., Nielsen, T. & Solheim, A. A new Late Weichselian and Holocene marine chronology for the western Svalbard slope 30,000–0 cal years BP. *Quaternary Science Reviews* **29**, 1301–1312 (2010). URL http://www.sciencedirect.com/science/article/pii/S0277379110000521.

[108] Junttila, J., Aagaard-Sørensen, S., Husum, K. & Hald, M. Late Glacial–Holocene clay minerals elucidating glacial history in the SW Barents Sea. *Marine Geology* **276**, 71–85 (2010).

[109] Knies, J., Kleiber, H.-P., Matthiessen, J., Müller, C. & Nowaczyk, N. Marine ice-rafted debris records constrain maximum extent of Saalian and Weichselian ice-sheets along the northern Eurasian margin. *Global and Planetary Change* **31**, 45–64 (2001).

[110] Kleiber, H. P., Knies, J. & Niessen, F. The Late Weichselian glaciation of the Franz Victoria Trough, northern Barents Sea: ice sheet extent and timing. *Marine Geology* **168**, 25–44 (2000).

[111] Kristensen, D. K., Rasmussen, T. L. & Koç, N. Palaeoceanographic changes in the northern Barents Sea during the last 16 000 years–new constraints on the last deglaciation of the Svalbard–Barents Sea Ice Sheet. *Boreas* **42**, 798–813 (2013).

[112] Landvik, J. Y. *et al.* The last glacial maximum of Svalbard and the Barents Sea area: ice sheet extent and configuration. *Quaternary Science Reviews* **17**, 43–75 (1998).

[113] Lantzsch, H. *et al.* Deglacial to Holocene history of ice-sheet retreat and bottom current strength on the western Barents Sea shelf. *Quaternary Science Reviews* **173**, 40–57 (2017). URL http://www.sciencedirect.com/science/article/pii/S0277379117300525.

[114] Lubinski, D. J. *et al.* The last deglaciation of the Franz Victoria Trough, northern Barents Sea. *Boreas* **25**, 89–100 (1996).

[115] Lubinski, D. J., Polyak, L. & Forman, S. L. Freshwater and Atlantic water inflows to the deep northern Barents and Kara seas since ca 13 ^{14}C ka:: foraminifera and stable isotopes. *Quaternary Science Reviews* **20**, 1851–1879 (2001).

[116] Lucchi, R. G. *et al.* Postglacial sedimentary processes on the Storfjorden and Kveithola trough mouth fans: Significance of extreme glacimarine sedimentation. *Global and Planetary Change* **111**, 309–326 (2013). URL http://www.sciencedirect.com/science/article/pii/S0921818113002270.

[117] Nielsen, T. & Rasmussen, T. L. Reconstruction of ice sheet retreat after the Last Glacial maximum in Storfjorden, southern Svalbard. *Marine Geology* **402**, 228–243 (2018).

[118] Ottesen, D., Dowdeswell, J. A. & Rise, L. Submarine landforms and the reconstruction of fast-flowing ice streams within a large Quaternary ice sheet: The 2500-km-long Norwegian-Svalbard margin (57\textdegree – 80\textdegree N). *GSA Bulletin* **117**, 1033 (2005). URL +http://dx.doi.org/10.1130/B25577.1.

[119] Patton, H. *et al.* Geophysical constraints on the dynamics and retreat of the Barents Sea ice sheet as a paleobenchmark for models of marine ice sheet deglaciation. *Reviews of Geophysics* **53**, 1051–1098 (2015). URL http://dx.doi.org/10.1002/2015RG000495.

[120] Pau, M. & Hammer, Ø. Sedimentary environments in the south-western Barents Sea during the last deglaciation and the Holocene: a case study outside the Ingøydjupet trough. *Polar Research* **35**, 23104 (2016). URL https://doi.org/10.3402/polar.v35.23104.

[121] Piasecka, E. D., Winsborrow, M. C. M., Andreassen, K. & Stokes, C. R. Reconstructing the retreat dynamics of the Bjørnøyrenna Ice Stream based on new 3D seismic data from the central Barents Sea. *Quaternary Science Reviews* **151**, 212–227 (2016). URL http://www.sciencedirect.com/science/article/pii/S027737911630347X.

[122] Polyak, B., Lehman, S. J., Gataullin, V. & Jull, A. J. T. Two-step deglaciation of the southeastern Barents Sea. *Geology* **23**, 567–571 (1995).

[123] Rüther, D. C., Mattingsdal, R., Andreassen, K., Forwick, M. & Husum, K. Seismic architecture and sedimentology of a major grounding zone system deposited by the Bjørnøyrenna Ice Stream during Late Weichselian deglaciation. *Quaternary Science Reviews* **30**, 2776–2792 (2011). URL http://www.sciencedirect.com/science/article/pii/S0277379111001831.

[124] Rüther, D. C. *et al.* Pattern and timing of the northwestern Barents Sea Ice Sheet deglaciation and indications of episodic Holocene deposition. *Boreas* **41**, 494–512 (2012). URL http://dx.doi.org/10.1111/j.1502-3885.2011.00244.x.

[125] Rüther, D. C., Winsborrow, M., Andreassen, K. & Forwick, M. Grounding line proximal sediment characteristics at a marine-based, late-stage ice stream margin. *Journal of Quaternary Science* **32**, 463–474 (2017). URL http://dx.doi.org/10.1002/jqs.2939.

[126] Salvigsen, O. Radiocarbon dated raised beaches in Kong Karls Land, Svalbard, and their consequences for the glacial history of the Barents Sea area. *Geografiska Annaler: Series A, Physical Geography* **63**, 283–291 (1981).

[127] Ślubowska-Woldengen, M. *et al.* Advection of Atlantic Water to the western and northern Svalbard shelf since 17,500 calyr BP. *Quaternary Science Reviews* **26**, 463–478 (2007).

[128] Svendsen, J. I., Elverhøy, A. & Mangerud, J. The retreat of the Barents Sea Ice Sheet on the western Svalbard margin. *Boreas* **25**, 244–256 (1996). URL http://dx.doi.org/10.1111/j.1502-3885.1996.tb00640.x.

[129] Winsborrow, M. C. M., Stokes, C. R. & Andreassen, K. Ice-stream flow switching during deglaciation of the southwestern Barents Sea. *GSA Bulletin* **124**, 275 (2012). URL +http://dx.doi.org/10.1130/B30416.1.

[130] Amundsen, H. B. *et al.* Late Weichselian–Holocene evolution of the high-latitude Andøya submarine Canyon, north-Norwegian continental margin. *Marine Geology* **363**, 1–14 (2015).

[131] Bugge, T. *Øvre lags geologi på kontinentalsokkelen utenfor Møre og Trøndelag* (IKU, Institutt for Kontinentalsokkelundersøkelser, 1980).

[132] Holtedahl, H. & Bjerkli, K. Late Quaternary sediments and stratigraphy on the continental shelf off Møre-Trøndelag, W. Norway. *Marine Geology* **45**, 179205–202226 (1982).

[133] King, E. L., Haflidason, H., Sejrup, H. P. & Løvlie, R. Glacigenic debris flows on the North Sea Trough Mouth Fan during ice stream maxima. *Marine Geology* **152**, 217–246 (1998). URL http://www.sciencedirect.com/science/article/pii/S0025322798000723.

[134] Laberg, J. S. *et al.* Late Quaternary palaeoenvironment and chronology in the Trænadjupet Slide area offshore Norway. *Marine Geology* **188**, 35–60 (2002). URL http://www.sciencedirect.com/science/article/pii/S0025322702002748.

[135] Laberg, J. S., Eilertsen, R. S., Salomonsen, G. R. & Vorren, T. O. Submarine push moraine formation during the early Fennoscandian Ice Sheet deglaciation. *Quaternary Research* **67**, 453–462 (2007). URL http://www.sciencedirect.com/science/article/pii/S003358940700018X.

[136] Laberg, J. S., Eilertsen, R. S. & Salomonsen, G. R. Deglacial dynamics of the Vestfjorden – Trænadjupet palaeo-ice stream, northern Norway. *Boreas* **47**, 225–237 (2018). URL http://dx.doi.org/10.1111/bor.12261.

[137] Nygård, A., Sejrup, H. P., Haflidason, H., Cecchi, M. & Ottesen, D. Deglaciation history of the southwestern Fennoscandian Ice Sheet between 15 and 13 ^{14}C ka BP. *Boreas* **33**, 1–17 (2004).

[138] Nygård, A. *et al.* Extreme sediment and ice discharge from marine-based ice streams: New evidence from the North Sea. *Geology* **35**, 395 (2007). URL +http://dx.doi.org/10.1130/G23364A.1.

[139] Rokoengen, K. & Bugge, T. Quaternary geology and deglaciation of the continental shelf off Troms, north Norway. *Boreas* **8**, 217–227 (1979).

[140] Rokoengen, K. & Frengstad, B. Radiocarbon and seismic evidence of ice-sheet extent and the last deglaciation on the mid-Norwegian continental shelf. *Norsk Geologisk Tidsskrift* **79**, 129–132 (1999).

[141] Sejrup, H. P., Nygård, A., Hall, A. M. & Haflidason, H. Middle and Late Weichselian (Devensian) glaciation history of south-western Norway, North Sea and eastern UK. *Quaternary Science Reviews* **28**, 370–380 (2009). URL http://www.sciencedirect.com/science/article/pii/S0277379108002990.

[142] Vorren, T. O. & Kristoffersen, Y. Late Quaternary glaciation in the south-western Barents Sea. *Boreas* **15**, 51–59 (1986). URL http://dx.doi.org/10.1111/j.1502-3885.1986.tb00742.x.

[143] Vorren, T. O. & Plassen, L. Deglaciation and palaeoclimate of the Andfjord-Vågsfjord area, North Norway. *Boreas* **31**, 97–125 (2002). URL http://dx.doi.org/10.1111/j.1502-3885.2002.tb01060.x.

[144] Trauth, M. H. TURBO2: A MATLAB simulation to study the effects of bioturbation on paleoceanographic time series. *Computers & geosciences* **61**, 1–10 (2013).

[145] Sejrup, H. P., Clark, C. D. & Hjelstuen, B. O. Rapid ice sheet retreat triggered by ice stream debuttressing: Evidence from the North Sea. *Geology* **44**, 355–358 (2016).

[146] Becker, L. W. M., Sejrup, H. P., Hjelstuen, B. O., Haflidason, H. & Dokken, T. M. Ocean-ice sheet interaction along the SE Nordic Seas margin from 35 to 15 ka BP. *Marine Geology* **402**, 99–117 (2018).

[147] Day, R., Fuller, M. & Schmidt, V. A. Hysteresis properties of titanomagnetites: grain-size and compositional dependence. *Physics of the Earth and planetary interiors* **13**, 260–267 (1977).

[148] Newton, A. J., Dugmore, A. J. & Gittings, B. M. Tephrabase: tephrochronology and the development of a centralised European database. *Journal of Quaternary Science* **22**, 737–743 (2007).

779 # Supplementary Figures

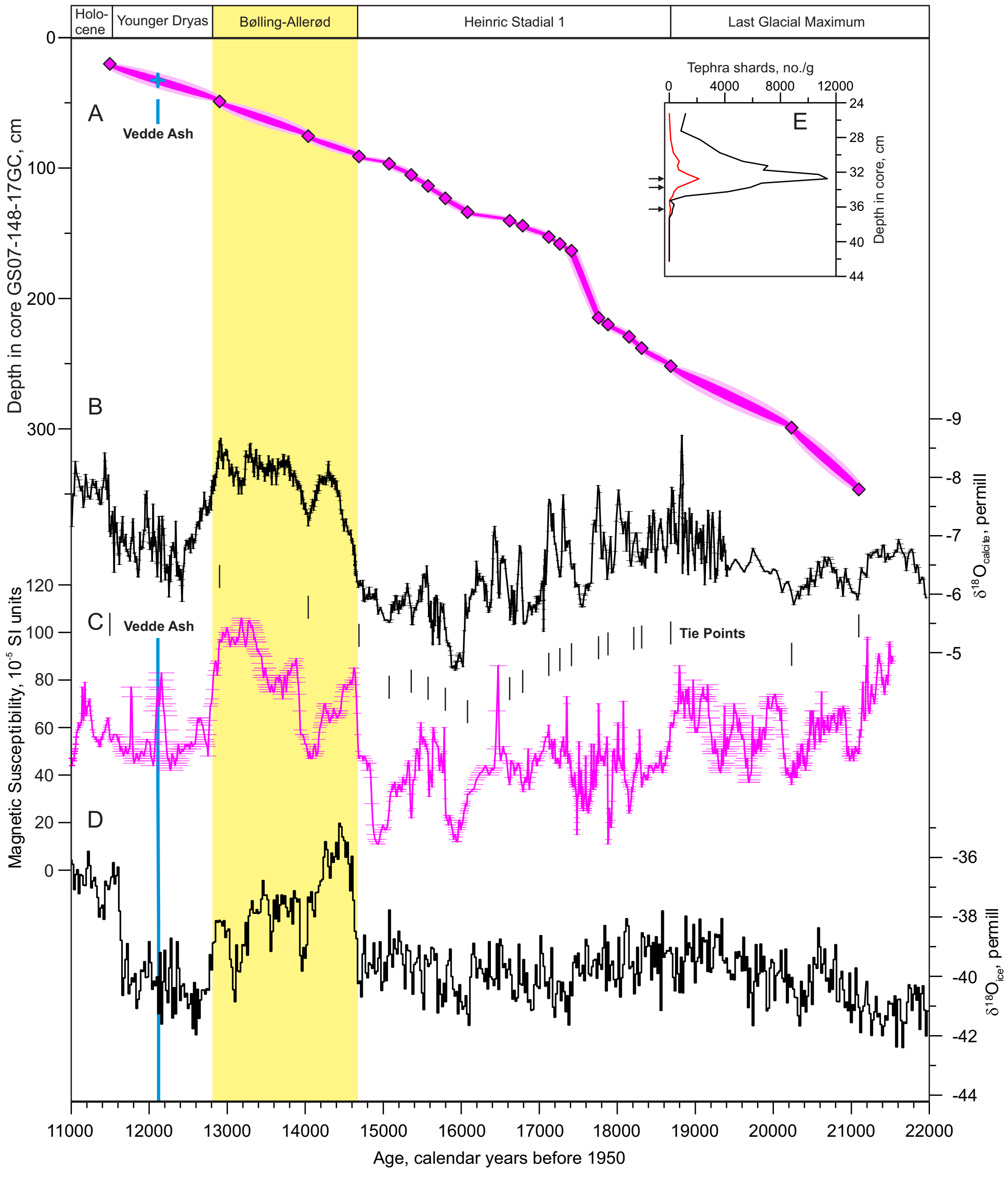

Supplementary Figure 1: Age-model of the Norwegian Sea core GS07-148-17GC. **A**, Age model constructed using the P_Sequence option in OxCal[67]. The dark- and light-colored bands represent the respective 68.2% and 95.4% credible intervals of the model. The model is made by defining tie-points (diamonds and vertical dashes between **(B)** and **(C)**) between the magnetic susceptibility record of core GS07-148-17GC **(C)** and the δ^{18}O record from Hulu cave **(B)**[28]. While the Bølling transition is associated with high sedimentation rates and deposition of plumites closer to the continental shelf edge and the ice sheet grounding line[89,107,116], core GS07-148-17GC is located in a more distal setting where the direct influence from sediment-laden meltwater plumes is less likely. The interval with high sedimentation rates centered at about 17.5 kyr cal BP is related to the deposition of a plumite sourced from the Norwegian Channel Ice Stream[79–81,145,146]. Horizontal error bars in **B-C** represent the 1σ uncertainty of the Oxcal-generated age-model for the respective records. **(D)**, The average of the δ^{18}O record from the Greenland summit ice cores (GISP2 and GRIP aligned on the GICC05 chronology[33]), which is plotted for reference. The peak occurrence of the Vedde Ash in core GS07-148-17GC and the Greenland ice cores is indicated by the blue line. Note that the Vedde Ash has not been used to constrain the GS07-148-17GC chronology, yet the difference in the Vedde Ash ages is only 10 years. **E**, The distribution of tephra shards found in core GS07-148-17GC, including rhyolitic (black) and basaltic (red) shards. Arrows mark levels sampled for geochemical analyses of tephra shards (Supplementary Fig. 4).

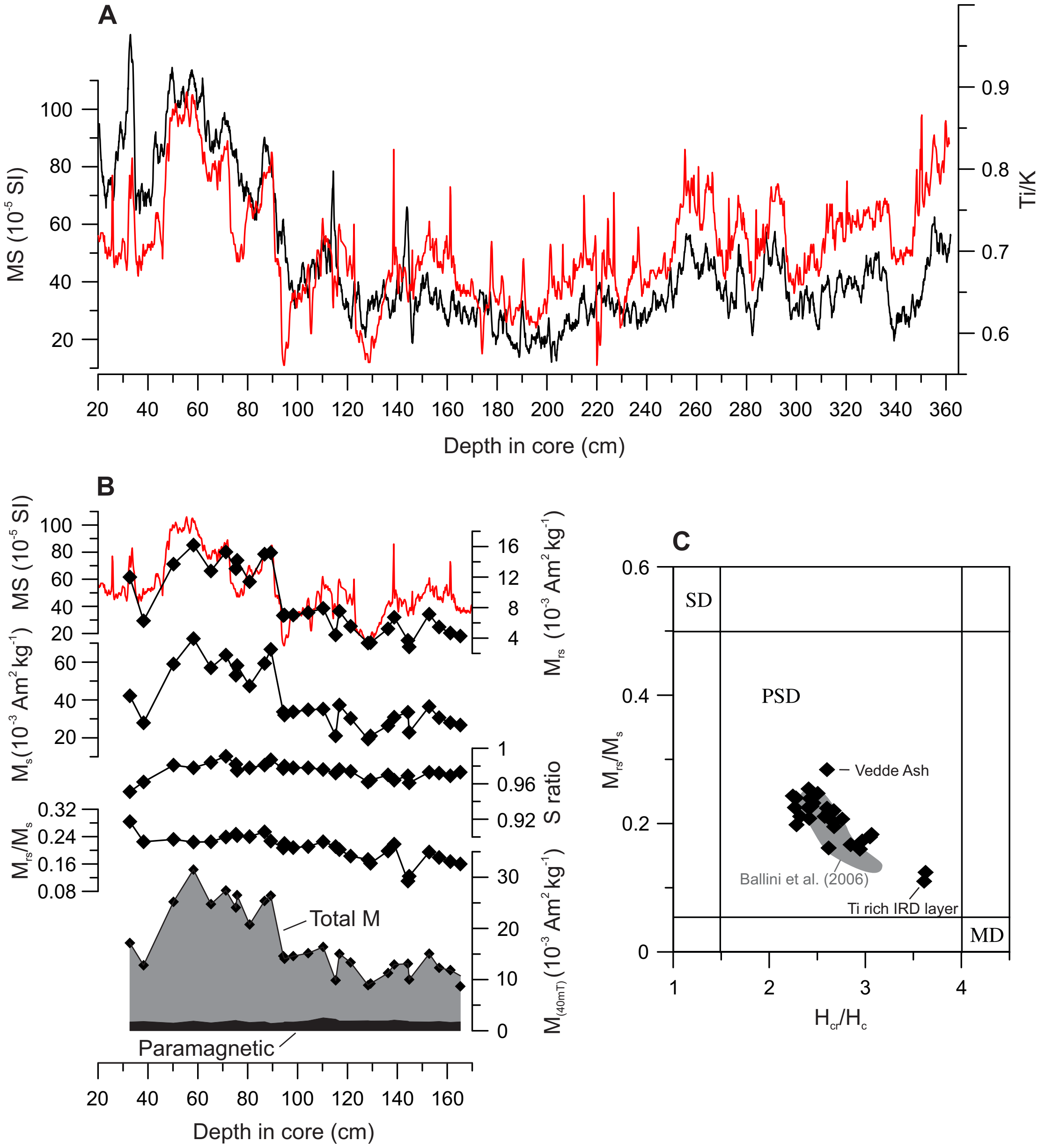

Supplementary Figure 2: Magnetic and geochemical parameters from the deglaciation interval in core GS07-148-17GC. A, Magnetic Susceptibility (MS)(red) and Ti/K ratio from Multi-sensor core logging and XRF core scanning (black, 11 point running mean). As found by Ballini et al.[71] during the MIS-3 interval, the MS and Ti/K closely co-vary also in the deglacial interval. B, black diamonds are hysteresis parameters from discrete sample measurements on a coercivity spectrometer (corrected for paramagnetic material). From the top: Saturation remanent magnetization (M_{rs}) and MS (red line). The M_{rs} and M_s closely track the bulk MS, as found in MIS-3[71]. An S-ratio (S=$-$IRM$_{-0.3T}$/IRM$_{0.5T}$) close to unity for all measured samples suggest that the ferromagnetic minerals are homogeneous and dominated by low coercivity minerals throughout the studied core interval, similar to the MIS-3[70,71]. The field strength necessary to reach saturation remanence is below 300 mT, pointing to magnetite or titanomagnetite as the main ferromagnetic mineral[70]. Additional thermomagnetic curves from representative MIS-3 samples[70,71] imply that the mineral carrying the SE-Norwegian Sea MS signal is low-Ti titanomagnetite. Slightly lower Mrs/Ms ratio in the HS1 interval of core GS07-148-17GC is consistent with the results of Ballini, et al.[71] suggesting that the magnetic grain sizes are slightly larger during stadials. The lowermost panel shows the total magnetic susceptibility (gray field, as measured and not corrected for paramagnetic material) at an induced field of 40 mT (M_{40mT}), and the corresponding paramagnetic contribution (black field). The low and relatively constant paramagnetic contribution to the total M demonstrates that the MS signal is driven by the concentration of ferromagnetic minerals. C, Day plot[147] showing that the magnetic grain sizes fall in the pseudo-single domain range, consistent with the results of Ballini et al.[71] (gray field).

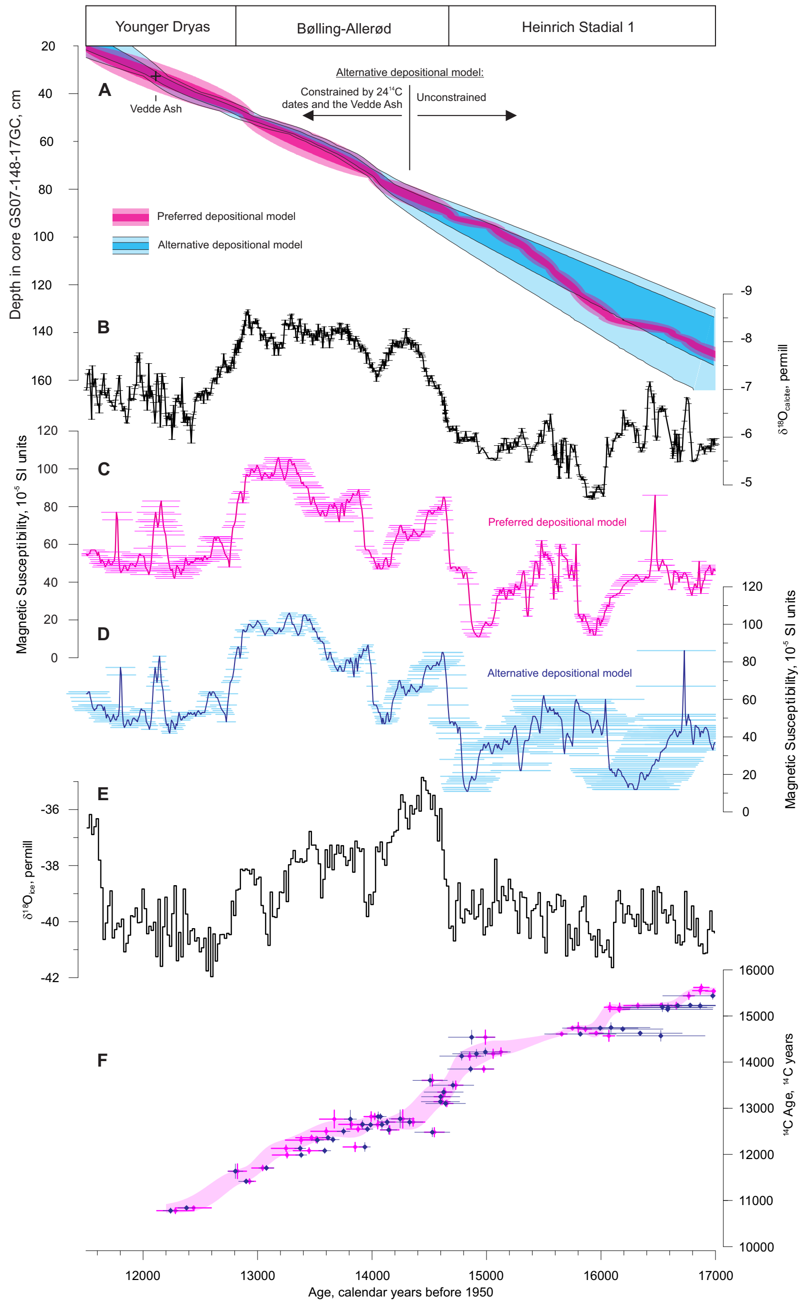

Supplementary Figure 3: Alternative depositional model of core GS07-148-17GC. **A**, comparison of the preferred depositon model (Magenta; Supplementary Fig. 1) and our alternative deposition model (cyan). Darker and lighter color represents the 68.2% and 95.4% credible intervals, respectively. The positions of the Vedde Ash, and the constrained and unconstrained segments of the models are indicated. **B**, The δ^{18}O record from Hulu cave as in Supplementary Fig. 1 [28]. **C-D**, the MS record of core GS07-148-17GC on the preferred (**C**, magenta) and alternative (**D**, blue) deposition model. The horizontal error bars in **B**, **C** and **D** represent the 1σ uncertainty of the Oxcal-generated deposition models for the respective records. **E**, the average of the δ^{18}O record from the Greenland summit ice cores (GISP2 and GRIP aligned on the GICC05 chronology [33]) plotted for reference. **F**, the ^{14}C ages of the Norwegian Sea compilation plotted both on our preferred chronology (magenta) and the alternative chronology (blue), the light pink field is the Norwegian Sea ^{14}C reconstruction.

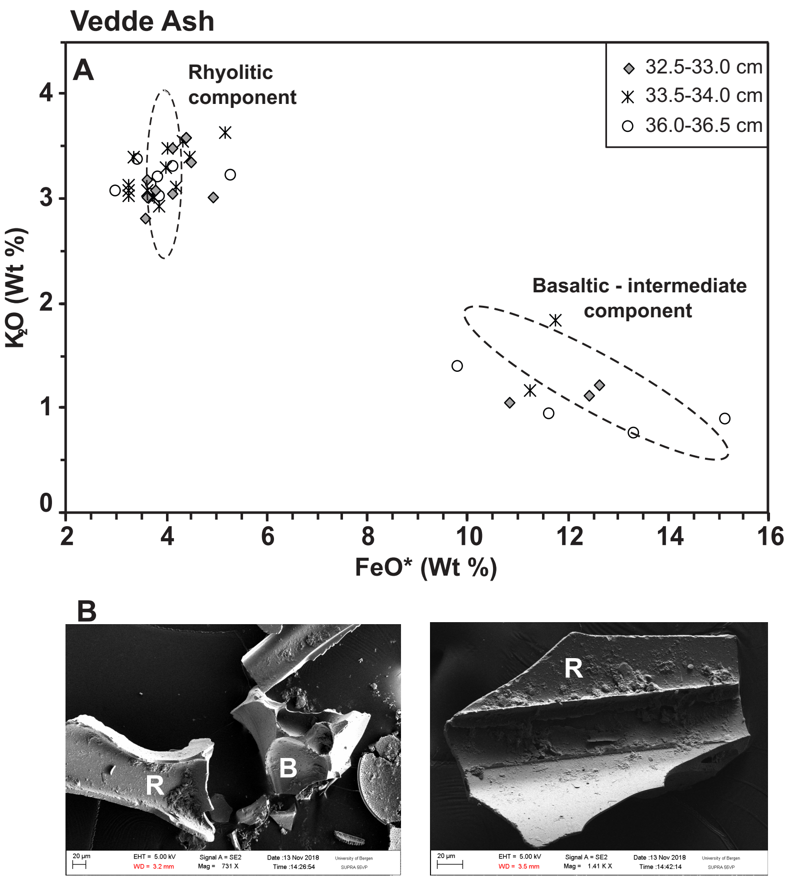

Supplementary Figure 4: The Vedde ash in core GS07-148-17GC. **A**, Bivariate plot of FeO* vs K_2O showing the results from all the data presented in the Supplementary data File. All data are normalized to a 100% total on a water and volatile-free basis for data set comparison (the Supplementary Data File contains the original non-normalized geochemical data). Total iron is expressed as FeO*. Compositional envelopes (dash lines) show the rhyolitic and basaltic-intermediate components of the Vedde Ash (from Tephrabase: www.tephrabase.org[148]). **B**, Scanning electron microscope images of glass shards from interval 32.5-33.0 cm depth in core GS07-148-17GC (B: basaltic glass, R: rhyolitic glass).

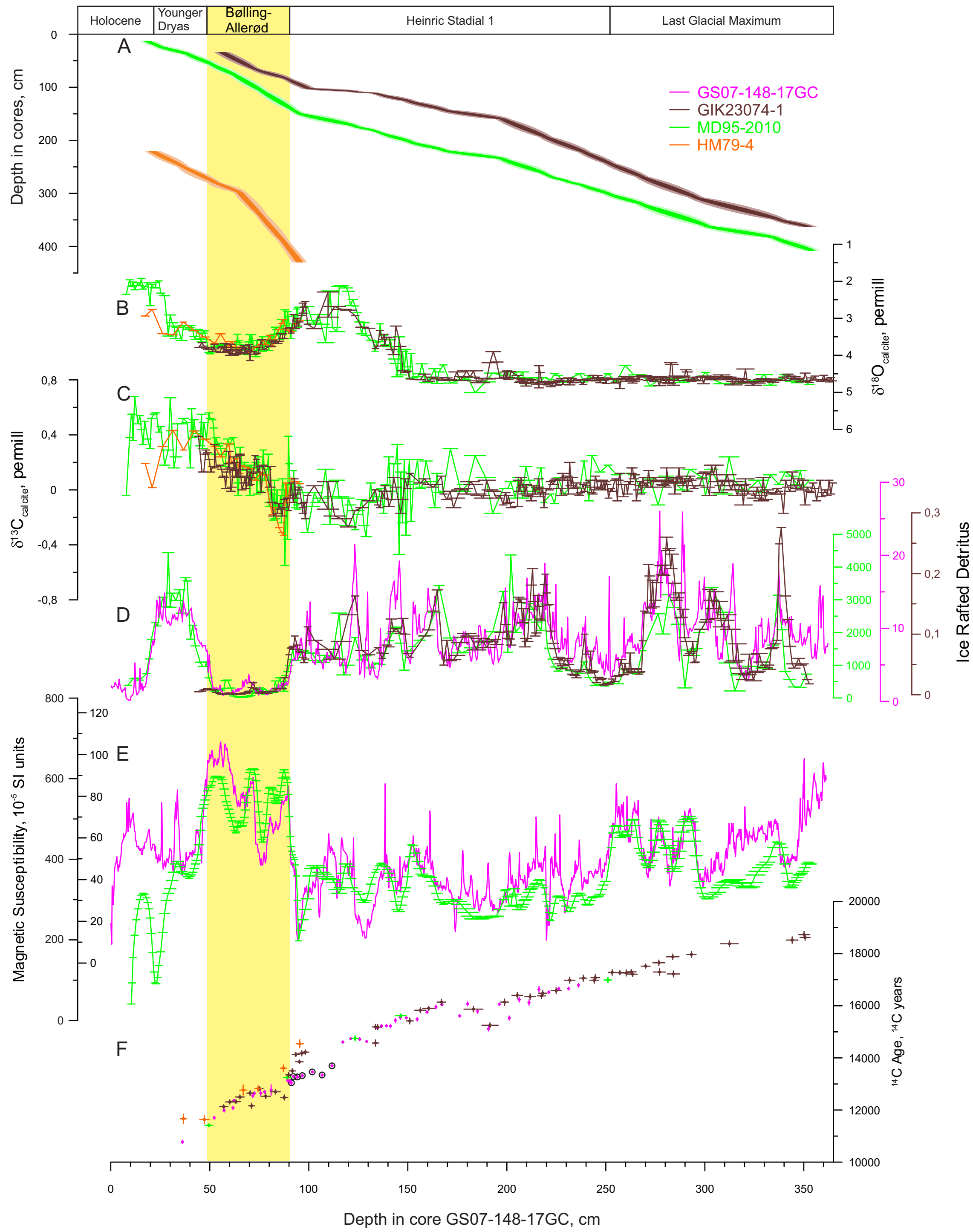

Supplementary Figure 5: Norwegian Sea data records plotted on GS07-148-17GC depth scale. **A**, Depth models of cores HM79-4, GIK23074-1 and MD95-2010 constructed using the P_Sequence option in OxCal [67]. Light-colored uncertainty envelopes represent the 95.4% quantiles, while darker colored represent the 68.2% quantiles of the depth model PDF. The models are made by defining tie-point between the cores and core GS07-148-17GC using the records of **(B)** δ^{18}O [32,34,35], **(C)** δ^{13}C [32,34,35], **(D)** IRD [32,34], and **(E)** magnetic susceptibility [32]. **F**, Compiled AMS ^{14}C [32,34–36]. Circles mark the dates that are excluded from further analysis due to distortion of the core stratigraphy from deep burrows (Supplementary Fig. 6). Horizontal error bars in **B-F** represent the 1σ uncertainty of the depth model for the respective cores.

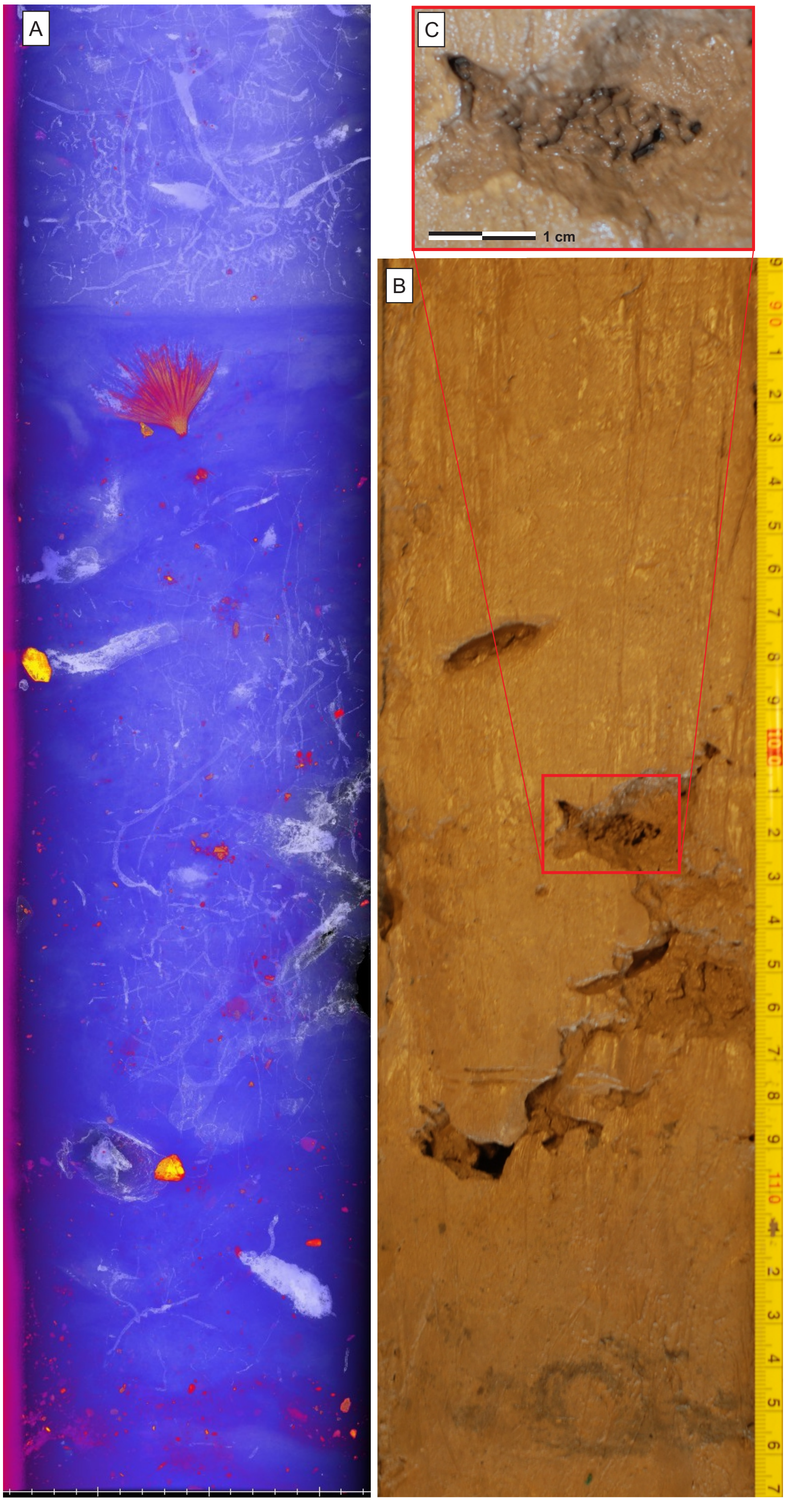

Supplementary Figure 6: Trace fossils and burrows between 83 and 117 cm depth in core GS07-148-17GC. **A**, Computed tomography radiograph with colour scheme chosen to emphasise trace fossils and burrows. White and light blue colours indicate low-density sediments and cavities, red and yellow colours mark high-density material. **B**, Photograph of the core surface showing open burrow tubes and cavities, **A** and **B** are aligned on the same depth scale. **C**,Close-up of burrow cavity containing ovoid pellets with the same density as the surrounding sediment. We assume these pellets were made by the burrowing organism.

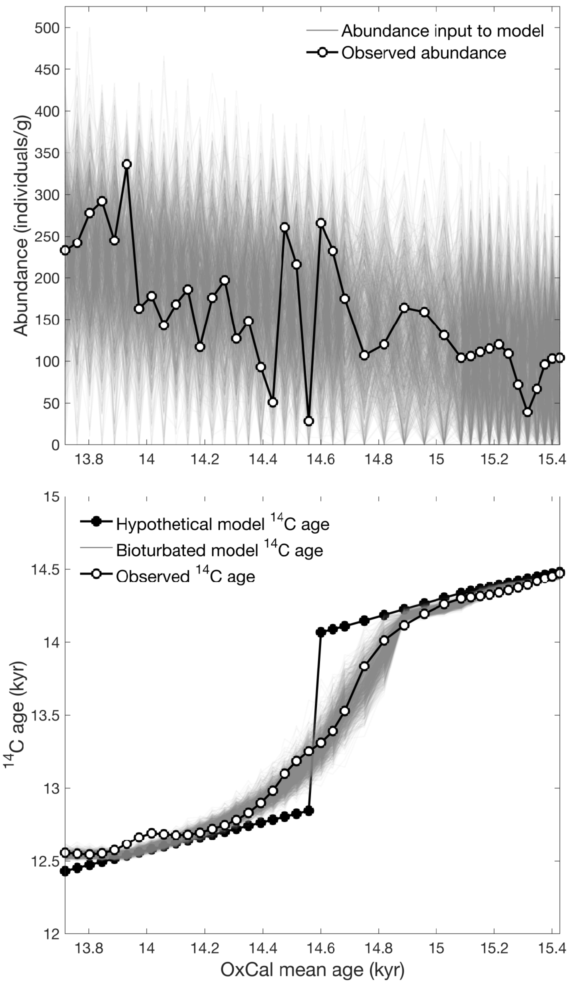

Supplementary Figure 7: The effect of bioturbation on the ^{14}C reconstruction at the Bølling transition. To assess the potential impact of bioturbation, we used the TURBO2 model[144] (Methods). As input we used 1,024 simulated abundance vectors (gray; top panel) generated as normally distributed random values centered on the best-fit linear trend and with the standard deviation of the observed abundance of foraminifera in core MD95-2210[32] (top panel). If we assume a constant mixed layer depth of 6 cm, then the observed change in ^{14}C age can be reproduced with reasonable accuracy in TURBO2 by invoking a hypothetical true ^{14}C age with an abrupt step change 14.56 kyr ago (lower panel). This result is not an attempt to infer the true ^{14}C age history, but rather to demonstrate that the effect of bioturbation would be to smear out the true event. As a consequence, our reconstruction is likely to overestimate the time scale of the EIS collapse and underestimate its contribution to the global MWP-1a.

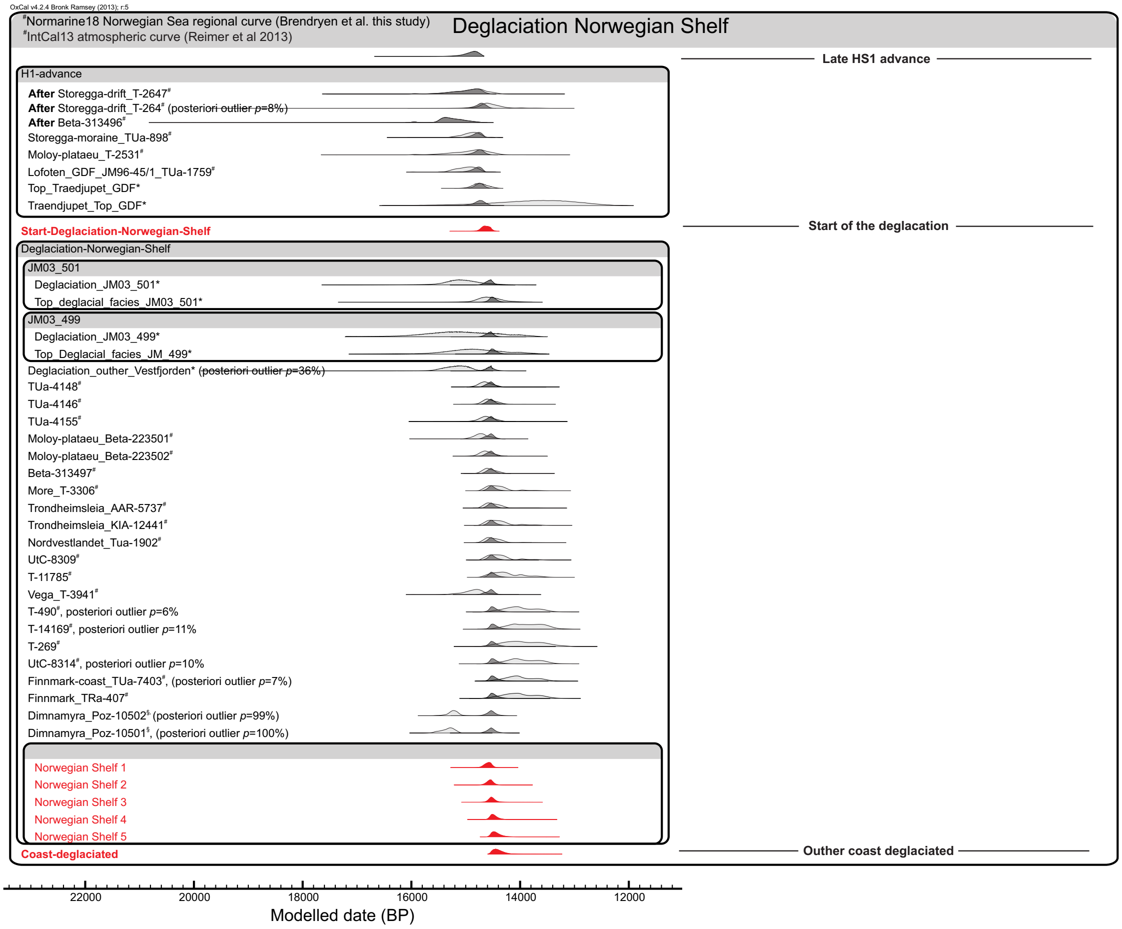

Supplementary Figure 8: Bayesian deglacial chronology of the Norwegian continental shelf. As prior information, all radiocarbon dates or probability density functions of sediment unit boundaries are grouped into phases according to geographical and/or stratigraphical context. A phase in this context refers to a retreat (or advance) of the ice sheet in a specific area. The phases are ordered in a sequence following the relative chronological order. The PDF's of unmodeled conventional ^{14}C dates are calibrated using the new Norwegian Sea ^{14}C age reconstruction (Fig. 2) and is shown as light gray. Dark gray mark the modeled posteriori PDF of the same dates. Red PDF's show the posteriori age probabilities of undated events that corresponds to reconstructed ice margins depicted in Fig. (1).

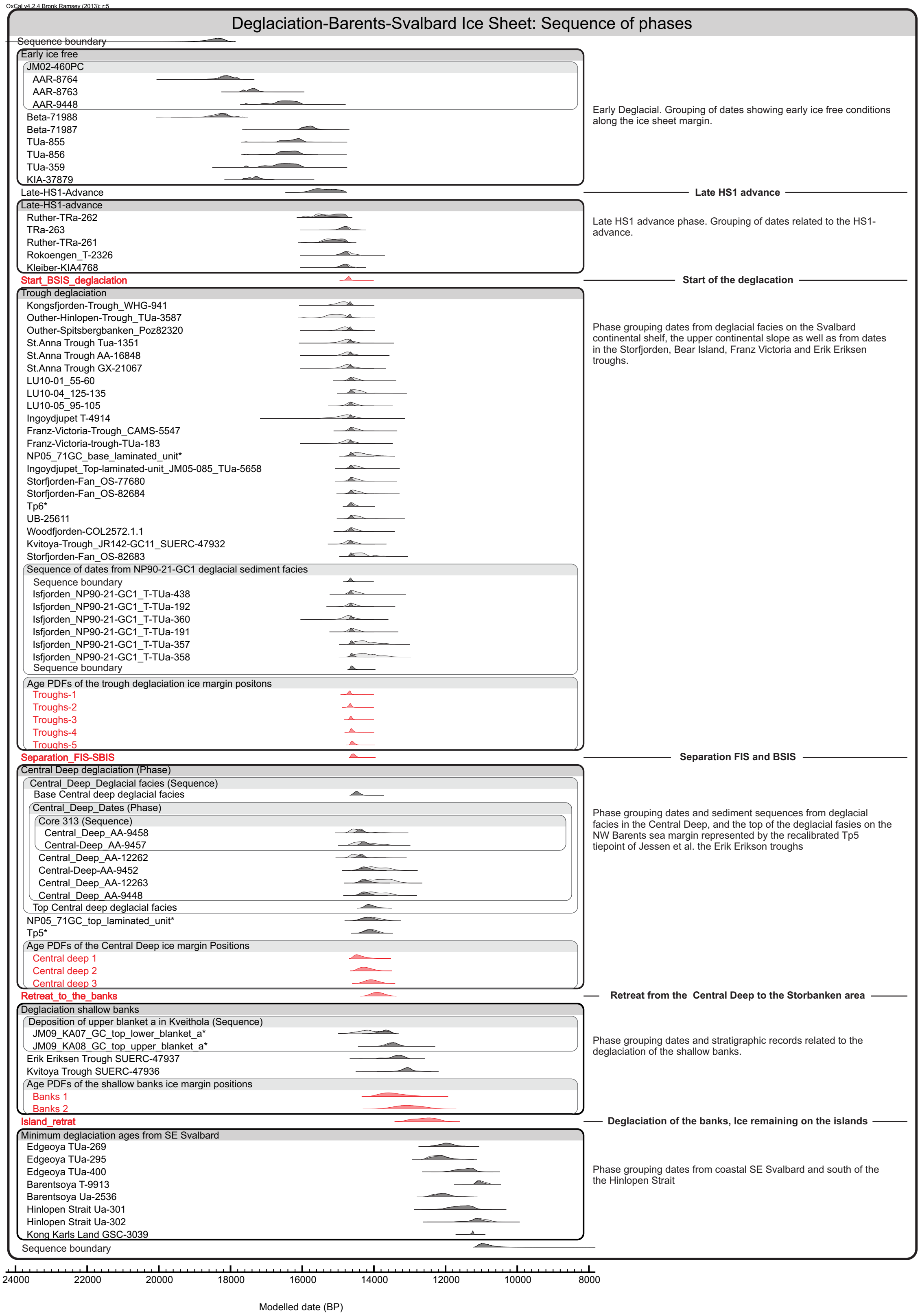

Supplementary Figure 9: Bayesian deglacial chronology of the Barents-Svalbard ice sheet. As prior information, all radiocarbon dates or probability density functions of sediment unit boundaries are grouped into phases according to geographical and/or stratigraphical context. A phase in this context refers to a retreat (or advance) of the ice sheet in a specific area. The phases are ordered in a sequence following the relative chronological order. The PDF's of unmodeled conventional ^{14}C dates are calibrated using the new Norwegian Sea ^{14}C age reconstruction (Fig. 2) and is shown as light gray. Dark gray mark the modeled posteriori PDF of the same dates. Red PDF's show the posteriori age probabilities of undated events that corresponds to reconstructed ice margins depicted in Fig. (1).

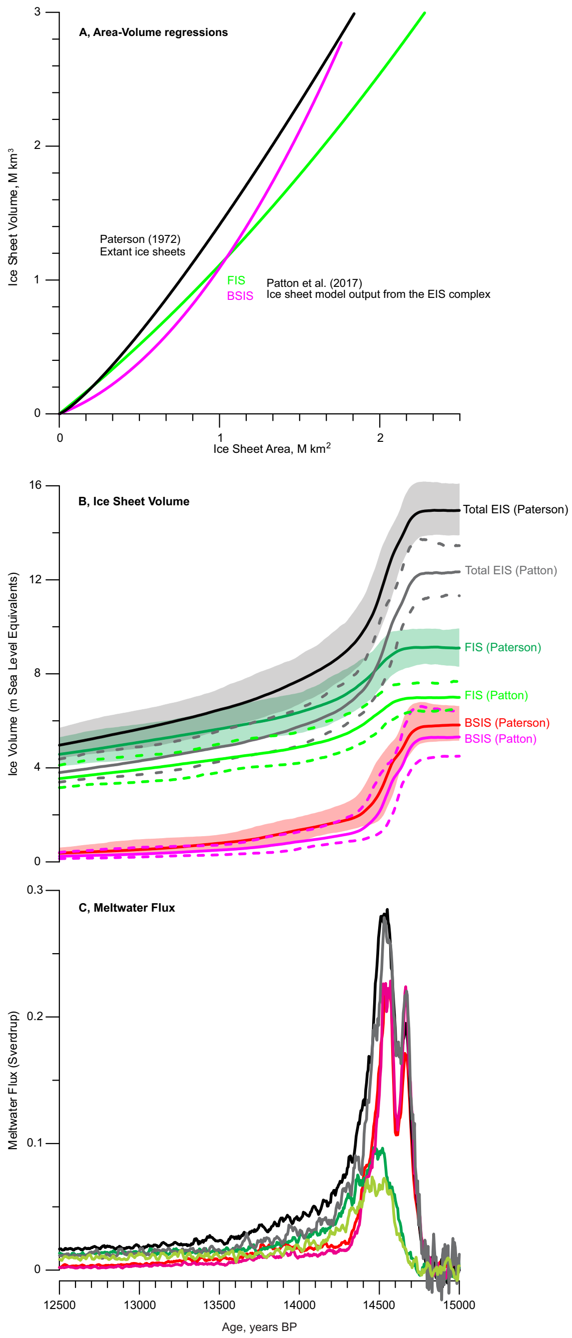

Supplementary Figure 10: Comparison between area-volume regressions. **A**, Regression lines of ice sheet area and volume data used to convert the EIS area reconstruction to volume with the regression of [39] trough six extant ice sheets (black) and regression lines (2nd order polynomial fits) through the EIS modeling output from [40] (green and purple). FIS, Fennoscandian Ice Sheet; BSIS, Barents Svalbard Ice Sheet; BIIS, British Isles Ice Sheet. **B**, Comparison of the EIS volume estimated by the regression of [39] and a 2nd order polynomial regression of ice sheet specific area-volume output from a transient model simulation of the growth and decay of the EIS complex of [40]. **C**, The corresponding meltwater fluxes. Color codes are the same as in **B**.